Benchmarking the Immersed Finite Element Method for Fluid-Structure Interaction Problems

Saswati Roy
Department of Engineering Science and Mechanics
The Pennsylvania State University
212 Earth and Engineering Sciences Building
University Park PA 16802 USA

Luca Heltai
Scuola Internazionale Superiore di Studi Avanzati
Via Bonomea 265
34136 Trieste, Italy

Francesco Costanzo*
Center for Neural Engineering
The Pennsylvania State University
W-315 Millennium Science Complex
University Park PA 16802 USA

June 4, 2013

Abstract

We present an implementation of a fully variational formulation of an immersed methods for fluid-structure interaction problems based on the finite element method. While typical implementation of immersed methods are characterized by the use of approximate Dirac delta distributions, fully variational formulations of the method do not require the use of said distributions. In our implementation the immersed solid is general in the sense that it is not required to have the same mass density and the same viscous response as the surrounding fluid. We assume that the immersed solid can be either viscoelastic of differential type or hyperelastic. Here we focus on the validation of the method via various benchmarks for fluid-structure interaction numerical schemes. This is the first time that the interaction of purely elastic compressible solids and an incompressible fluid is approached via an immersed method allowing a direct comparison with established benchmarks.

Keywords: Fluid-Structure Interaction; Fluid-Structure Interaction Benchmarking; Immersed Boundary Methods; Immersed Finite Element Method; Finite Element Immersed Boundary Method

1 Introduction

Immersed methods for fluid structure interaction (FSI) problems were pioneered by Peskin and his co-workers (Peskin, 1977, 2002). They proposed an approach called the immersed boundary

*Corresponding Author. Email: Francesco Costanzo <costanzo@engr.psu.edu>; Tel.: +1 814 863-2030; Fax: +1 814 865-9974

method (IBM), in which the equations governing the fluid motion have body force terms describing the FSI. The equations are integrated via a finite difference (FD) method and the body force terms are computed by modeling the solid body as a network of elastic fibers. As such, this system of forces has singular support (the *boundary* in the method's name) and is implemented via Dirac-δ distributions. The configuration of the fiber network is represented via a discrete set of points whose motion is then related to that of the fluid again via Dirac-δ distributions. In the numerical implementation of this method the Dirac-δ distributions are aproximated as *functions*.

Immersed methods based on the finite element method (FEM) has been formulated by various authors (Boffi and Gastaldi, 2003; Boffi et al., 2008; Wang and Liu, 2004; Zhang et al., 2004a). Boffi and Gastaldi (2003) were the first to show that a variational approach to immersed methods does not necessitate the approximation of Dirac-δ distributions as they naturally disappears in the weak formulation. The thrust of the work by Wang and Liu (2004) and Zhang et al. (2004a) was to remove the requirement that the immersed solid be a "boundary." While they proposed an approach applicable to solid bodies of general topological and constitutive characteristics they maintained the use of approximated Dirac-δ distribution through a strategy called the reproducing kernel particle method (RKPM).

Recently, Heltai and Costanzo (2012) proposed a generalization of the approach by Boffi et al. (2008) in which a fully variational FEM formulation is shown to be applicable to problems with immersed bodies of general topological and constitutive characteristics and without the use of Dirac-δ distributions. The formulation by Heltai and Costanzo (2012) focused on the construction of natural interpolation operators between the fluid and the solid discrete spaces that guarantee semi-discrete stability estimates and strong consistency. In this paper we discuss some details of the implementation of the approach in Heltai and Costanzo (2012) and present some numerical results toward a full validation of the method.

2 Formulation

2.1 Basic notation and governing equations

Referring to Fig. 1, we consider the interaction between a body with current configuration B_t

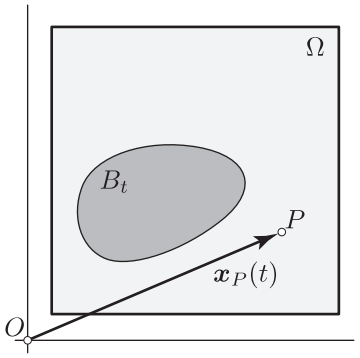

Figure 1: Current configuration B_t of a body $\mathscr{B}$ immersed in a fluid occupying the domain Ω.

immersed in a fluid occupying the domains $\Omega \setminus B_t$, where Ω is a fixed control volume. The body B_t has reference configuration $\mathscr{B}$. The boundaries of Ω and B_t, with outer unit normals $\boldsymbol{m}$ and $\boldsymbol{n}$, respectively, are $\partial\Omega$ and ∂B_t. We denote the position of points of $\mathscr{B}$ in B by $\boldsymbol{s}$, whereas we denote the position at time t of a generic point $P \in \Omega$ by $\boldsymbol{x}_P(t)$. A motion of $\mathscr{B}$ is a diffeomorphism $\boldsymbol{\zeta} : B \to B_t$, $\boldsymbol{x} = \boldsymbol{\zeta}(\boldsymbol{s}, t)$, with $\boldsymbol{s} \in B$, $\boldsymbol{x} \in \Omega$, and $t \in [0, T)$, with $T > 0$.

The spatial (or Eulerian) form of the balance of mass and balance of momentum are

$$\frac{\partial \rho}{\partial t} + \nabla \cdot (\rho \boldsymbol{u}) = 0, \quad \boldsymbol{x} \in \Omega \setminus (\partial\Omega \cup \partial B_t), \tag{1}$$

$$\nabla \cdot \mathsf{T} + \rho \boldsymbol{b} = \rho \left[\frac{\partial \boldsymbol{u}}{\partial t} + (\nabla \boldsymbol{u}) \boldsymbol{u} \right], \quad \boldsymbol{x} \in \Omega \setminus (\partial\Omega \cup \partial B_t), \tag{2}$$

where, for $\boldsymbol{x} \in \Omega$ and $t \in [0, T)$, $\rho(\boldsymbol{x}, t)$ is the mass density distribution, $\boldsymbol{u}(\boldsymbol{x}, t)$ is the velocity, $\mathsf{T}(\boldsymbol{x}, t)$ is the Cauchy stress, $\boldsymbol{b}(\boldsymbol{x}, t)$ is the external force density per unit mass acting on the system, and where ∇ and $(\nabla \cdot)$ denote the gradient and divergence operators, respectively. The above equations are understood to hold both for the solid and the fluid. The distinction between solid and fluid is enforced via their constitutive equations. In addition to Eqs. (1) and (2), we demand that the velocity field be continuous) and that the jump condition of the balance of linear momentum be satisfied across ∂B_t:

$$\boldsymbol{u}(\check{\boldsymbol{x}}^+, t) = \boldsymbol{u}(\check{\boldsymbol{x}}^-, t) \quad \text{and} \quad \mathsf{T}(\check{\boldsymbol{x}}^+, t)\boldsymbol{n} = \mathsf{T}(\check{\boldsymbol{x}}^-, t)\boldsymbol{n}, \quad \check{\boldsymbol{x}} \in \partial B_t, \tag{3}$$

where the superscripts $-$ and $+$ denote limits as $\boldsymbol{x} \to \check{\boldsymbol{x}}$ from within and without B_t, respectively.

We denote by $\partial\Omega_D$ and $\partial\Omega_N$ the subsets of $\partial\Omega$ where Dirichlet and Neumann boundary data are prescribed, respectively. The domains $\partial\Omega_D$ and $\partial\Omega_N$ are such that

$$\partial\Omega = \partial\Omega_D \cup \partial\Omega_N \quad \text{and} \quad \partial\Omega_D \cap \partial\Omega_N = \emptyset. \tag{4}$$

We denote by $\boldsymbol{u}_g(\boldsymbol{x}, t)$, with $\boldsymbol{x} \in \partial\Omega_D$, and by $\boldsymbol{\tau}_g(\boldsymbol{x}, t)$, with $\boldsymbol{x} \in \partial\Omega_N$, the prescribed values of velocity (Dirichlet data) and traction (Neumann data), respectively, i.e.,

$$\boldsymbol{u}(\boldsymbol{x}, t) = \boldsymbol{u}_g(\boldsymbol{x}, t), \quad \text{for } \boldsymbol{x} \in \partial\Omega_D, \quad \text{and} \quad \mathsf{T}(\boldsymbol{x}, t)\boldsymbol{m}(\boldsymbol{x}, t) = \boldsymbol{\tau}_g(\boldsymbol{x}, t), \quad \text{for } \boldsymbol{x} \in \partial\Omega_N, \tag{5}$$

where the subscript g stands for 'given.'

2.2 Constitutive response of the fluid.

The fluid is assumed to be linear viscous and incompressible with uniform mass density ρ_{f}. Denoting by $\hat{\mathsf{T}}_{\mathrm{f}}$ the constitutive response function of the Cauchy stress of the fluid, we have

$$\hat{\mathsf{T}}_{\mathrm{f}} = -p\mathsf{I} + \hat{\mathsf{T}}^v_{\mathrm{f}} \quad \text{and} \quad \hat{\mathsf{T}}^v_{\mathrm{f}} = \mu_{\mathrm{f}}\big(\nabla \boldsymbol{u} + \nabla \boldsymbol{u}^{\mathrm{T}}\big) \tag{6}$$

where the subscript f stands for 'fluid,' p is the pressure of the fluid, I is the identity tensor, $\hat{\mathsf{T}}^v_{\mathrm{f}}$ the viscous component of the stress, and $\mu_{\mathrm{f}} > 0$ is the dynamic viscosity of the fluid. Incompressibility demands that ρ_{f} be constant so for $\boldsymbol{x} \in \Omega \setminus B_t$, Eq. (1) reduces to the kinematic constraint equation $\nabla \cdot \boldsymbol{u} = 0$ and p takes on the role of a Lagrange multiplier for the enforcement of this constraint.

2.3 Constitutive response of the solid.

We assume that the body $\mathscr{B}$ is viscoelastic of differential type. The response function for the Cauchy stress of the solid is assumed to have the following form:

$$\hat{\mathsf{T}}_{\mathrm{s}} = \hat{\mathsf{T}}^e_{\mathrm{s}} + \hat{\mathsf{T}}^v_{\mathrm{s}}, \tag{7}$$

where the subscript s stands for 'solid,' $\hat{\mathsf{T}}^e_{\mathrm{s}}$ and $\hat{\mathsf{T}}^v_{\mathrm{s}}$ are the elastic and viscous parts of $\hat{\mathsf{T}}_{\mathrm{s}}$, respectively. The viscous part of the behavior is assumed to be of the same type as that of the fluid:

$$\hat{\mathsf{T}}^v_{\mathrm{s}} = \mu_{\mathrm{s}}\big(\nabla \boldsymbol{u} + \nabla \boldsymbol{u}^{\mathrm{T}}\big), \tag{8}$$

where $\mu_{\mathrm{s}} \geq 0$ is the dynamic viscosity of the solid. We do include the possibility that μ_{s} might be equal to zero, in which case the solid behaves in a purely elastic manner. We assume $\hat{\mathsf{T}}_{\mathrm{s}}^{e}$ to originate from a strain energy potential. Let the first Piola-Kirchhoff stress tensor, denoted by P and defined as (see, e.g., Gurtin et al., 2010):

$$\mathsf{P} = J\mathsf{T}\mathsf{F}^{-\mathrm{T}}, \tag{9}$$

where $J = \det \mathsf{F} > 0$, and the tensor $\mathsf{F} = \partial \boldsymbol{\zeta}(\boldsymbol{s}, t)/\partial \boldsymbol{s}$ is the deformation gradient. Hence, letting $\hat{\mathsf{P}}_{\mathrm{s}}^{e} = J\hat{\mathsf{T}}_{\mathrm{s}}^{e}F^{-\mathrm{T}}$ denote the elastic part of the first Piola-Kirchhoff stress, we assume that there exists a function $\hat{W}_{\mathrm{s}}^{e}(\mathsf{F})$ such that

$$\hat{\mathsf{P}}_{\mathrm{s}}^{e} = \frac{\partial \hat{W}_{\mathrm{s}}^{e}(\mathsf{F})}{\partial \mathsf{F}}, \tag{10}$$

where $\hat{W}_{\mathrm{s}}^{e}$ is the volume density of the elastic strain energy of the solid. If the solid is incompressible, its stress response is determined by deformation only up to a hydrostatic component. In this case, the constitutive response function for the solid has the form

$$\hat{\mathsf{T}}_{\mathrm{s}} = -p\mathsf{I} + \hat{\mathsf{T}}_{\mathrm{s}}^{e} + \hat{\mathsf{T}}_{\mathrm{s}}^{v}, \tag{11}$$

where p is a Lagrange multiplier enforcing incompressibility, $\hat{\mathsf{T}}_{\mathrm{s}}^{v}$ is given by Eq. (8), and $\hat{\mathsf{T}}_{\mathrm{s}}^{e}$ is obtained from Eq. (10).

2.3.1 Elastic strain energy and dissipation

While more general cases can be considered, we assume that $\hat{W}_{\mathrm{s}}^{e}(\mathsf{F})$ is a C^1 convex function over the set of second order tensor with positive determinant. As far as the viscous part of the behavior is concerned, we have already assumed that $\mu_{\mathrm{f}} > 0$ and $\mu_{\mathrm{s}} \geq 0$. These conditions imply that

$$\hat{\mathsf{T}}_{\mathrm{f}}^{v} \cdot \mathsf{L} > 0, \qquad \hat{\mathsf{T}}_{\mathrm{s}}^{v} \cdot \mathsf{L} \geq 0 \tag{12}$$

for all $\nabla \boldsymbol{u} \neq \mathsf{0}$. Equations (12) imply that the viscous part of the behavior is dissipative.

2.3.2 Mass density distribution

As a last aspect of the formulation related to constitutive behavior, we will denote by

$$\rho_{\mathrm{s}_0} = \rho_{\mathrm{s}_0}(\boldsymbol{s}), \quad \boldsymbol{s} \in B, \tag{13}$$

the referential (or Lagrangian) description of the mass density of the solid. While Eq. (1) holds for the solid as well as the fluid, the local form of the balance of mass for a solid is typically expressed in Lagrangian form as follows:

$$\rho_{\mathrm{s}_0}(\boldsymbol{s}) = \rho_{\mathrm{s}}(\boldsymbol{x}, t)\big|_{\boldsymbol{x}=\boldsymbol{\zeta}(\boldsymbol{s},t)} J(\boldsymbol{s}, t), \quad \boldsymbol{s} \in B, \tag{14}$$

where $\rho_{\mathrm{s}}(\boldsymbol{x}, t)$ is the spatial description of the mass density of the solid. We will indicate the general mass density of the system with $\rho = \rho(\boldsymbol{x}, t)$, with the underlying assumption that

$$\rho(\boldsymbol{x}, t) = \begin{cases} \rho_{\mathrm{f}}, & \text{for } \boldsymbol{x} \in \Omega \setminus B_t, \\ \rho_{\mathrm{s}}(\boldsymbol{x}, t), & \text{for } \boldsymbol{x} \in B_t, \end{cases} \tag{15}$$

where, as stated earlier, ρ_{f} is a constant.

3 Abstract Variational Formulation

The presentation in this section is an abbreviated exposition of the material in Heltai and Costanzo (2012), which should be consulted for details and proofs.

As is typical in FSI problems, the kinematic of the fluid is completely expressed in terms of the velocity field whereas the kinematics of the solid is in terms of the deformation gradient of the motion. To relate the velocity field and the motion of the fluid we introduce an intermediate kinematics descriptors, which is then used as the principal unknown describing the motion of the solid. Such a descriptor is the displacement field, denoted by $\boldsymbol{w}$ and defined as

$$\boldsymbol{w}(\boldsymbol{s},t) := \boldsymbol{\zeta}(\boldsymbol{s},t) - \boldsymbol{s}, \quad \boldsymbol{s} \in B, \tag{16}$$

which implies

$$\dot{\boldsymbol{w}}(\boldsymbol{s},t) = \boldsymbol{u}(\boldsymbol{x},t)\big|_{\boldsymbol{x}=\boldsymbol{\zeta}(\boldsymbol{s},t)}. \tag{17}$$

We remark that the practical enforcement of Eq. (17) is crucial to distinguish an immersed method from another. In the original IBM, Eq. (17) was enforced via Dirac-δ distributions. In the present formulation, we enforce Eq. (17) in a fully variational way.

3.1 Functional setting

The principal unknowns of our fluid-structure interaction problem are the fields

$$\boldsymbol{u}(\boldsymbol{x},t), \quad p(\boldsymbol{x},t), \quad \text{and} \quad \boldsymbol{w}(\boldsymbol{s},t), \quad \text{with } \boldsymbol{x} \in \Omega,\ \boldsymbol{s} \in B, \text{ and } t \in [0,T). \tag{18}$$

The functional spaces for these fields are

$$\boldsymbol{u} \in \mathscr{V} = H^1_D(\Omega)^d := \Big\{ \boldsymbol{u} \in L^2(\Omega)^d \,\big|\, \nabla_{\boldsymbol{x}}\boldsymbol{u} \in L^2(\Omega)^{d\times d}, \boldsymbol{u}|_{\partial\Omega_D} = \boldsymbol{u}_g \Big\}, \tag{19}$$

$$p \in \mathscr{Q} := L^2(\Omega), \tag{20}$$

$$\boldsymbol{w} \in \mathscr{Y} := \Big\{ \boldsymbol{w} \in L^2(B)^d \,\big|\, \nabla_{\boldsymbol{s}}\boldsymbol{w} \in L^\infty(B)^{d\times d} \Big\}, \tag{21}$$

where $\nabla_{\boldsymbol{x}}$ and $\nabla_{\boldsymbol{s}}$ denote the gradient operators relative to $\boldsymbol{x}$ and $\boldsymbol{s}$, respectively.

For convenience, we will use a prime to denote partial differentiation with respect to time:

$$\boldsymbol{u}'(\boldsymbol{x},t) := \frac{\partial \boldsymbol{u}(\boldsymbol{x},t)}{\partial t} \quad \text{and} \quad \boldsymbol{w}'(\boldsymbol{s},t) := \frac{\partial \boldsymbol{w}(\boldsymbol{s},t)}{\partial t}. \tag{22}$$

Equations (19) and (20) imply that the fields $\boldsymbol{u}$ and p are defined everywhere in Ω. Because $\boldsymbol{u}$ is defined everywhere in Ω, the function $\hat{\mathsf{T}}^v_{\mathrm{f}}$ is defined everywhere in Ω as well. For consistency, we must also extend the domain of definition of the mass density of the fluid. Hence, we formally assume that

$$\rho_{\mathrm{f}} \in L^\infty(\Omega). \tag{23}$$

Referring to Eq. (19), the function space for the velocity test functionsis $\mathscr{V}_0$ defined as

$$\mathscr{V}_0 = H^1_0(\Omega)^d := \Big\{ \boldsymbol{v} \in L^2(\Omega)^d \,\big|\, \nabla_{\boldsymbol{x}}\boldsymbol{v} \in L^2(\Omega)^{d\times d}, \boldsymbol{v}|_{\partial\Omega_D} = \boldsymbol{0} \Big\}. \tag{24}$$

Remark 1 (Functional spaces for time derivatives). In general, the functions $\boldsymbol{u}'$ and $\boldsymbol{w}'$ are not expected to be in $\mathscr{V}$ and $\mathscr{Y}$, respectively. The regularity of $\boldsymbol{u}'$ is related to the regularity of body force field density $\boldsymbol{b}$ and of the boundary conditions. The field $\boldsymbol{b}$ is typically assumed to be in $H^{-1}(\Omega)$. However, since the regularity of $\boldsymbol{b}$ is not the only factor at play, as was done in Heltai and Costanzo (2012), we take $\boldsymbol{u}'$ to be in a pivot space $\mathscr{H}_V$ such that

$$\mathscr{V} \subseteq \mathscr{H}_V \subseteq \mathscr{H}_V^* \subseteq \mathscr{V}^*, \tag{25}$$

where $\mathscr{H}_V^*$ and $\mathscr{V}^*$ are the dual spaces of $\mathscr{H}_V$ and $\mathscr{V}$, respectively. As far as $\boldsymbol{w}'$ is concerned, as was shown in Heltai and Costanzo (2012), under the assumption that $J > J_0 > 0$ and for $\boldsymbol{w} \in \mathscr{Y}$ and $\boldsymbol{u} \in \mathscr{V}$, we can show that $\boldsymbol{w}'$ is an element of $H^1(B)^d$.

3.2 Governing equations: incompressible solid

When the solid is incompressible, the mass density of both the fluid and the solid are constant and the governing equations can be given the following form (Heltai and Costanzo, 2012):

$$\begin{aligned}
&\int_\Omega \rho_{\mathrm{f}}\big[\boldsymbol{u}' + (\nabla_{\boldsymbol{x}}\boldsymbol{u})\boldsymbol{u} - \boldsymbol{b}\big]\cdot\boldsymbol{v}\,\mathrm{d}v - \int_\Omega p(\nabla_{\boldsymbol{x}}\cdot\boldsymbol{v})\,\mathrm{d}v + \int_\Omega \hat{\mathsf{T}}_{\mathrm{f}}^v\cdot\nabla_{\boldsymbol{x}}\boldsymbol{v}\,\mathrm{d}v - \int_{\partial\Omega_N}\boldsymbol{\tau}_g\cdot\boldsymbol{v}\,\mathrm{d}a \\
&+ \int_B \big\{[\rho_{\mathrm{s}_0}(\boldsymbol{s}) - \rho_{\mathrm{f}}J(\boldsymbol{s},t)]\big\{\boldsymbol{u}'(\boldsymbol{x},t) + \big[\nabla_{\boldsymbol{x}}\boldsymbol{u}(\boldsymbol{x},t)\big]\boldsymbol{u}(\boldsymbol{x},t) - \boldsymbol{b}(\boldsymbol{x},t)\big\}\cdot\boldsymbol{v}(\boldsymbol{x})\big|_{\boldsymbol{x}=\boldsymbol{\zeta}(\boldsymbol{s},t)}\,\mathrm{d}V \\
&\qquad + \int_B J(\boldsymbol{s},t)\big(\hat{\mathsf{T}}_{\mathrm{s}}^v - \hat{\mathsf{T}}_{\mathrm{f}}^v\big)\cdot\nabla_{\boldsymbol{x}}\boldsymbol{v}(\boldsymbol{x})\big|_{\boldsymbol{x}=\boldsymbol{\zeta}(\boldsymbol{s},t)}\,\mathrm{d}V \\
&\qquad\qquad + \int_B \hat{\mathsf{P}}_{\mathrm{s}}^e\,\mathsf{F}^{\mathrm{T}}(\boldsymbol{s},t)\cdot\nabla_{\boldsymbol{x}}\boldsymbol{v}(\boldsymbol{x})\big|_{\boldsymbol{x}=\boldsymbol{\zeta}(\boldsymbol{s},t)}\,\mathrm{d}V = 0 \quad \forall\boldsymbol{v}\in\mathscr{V}_0,
\end{aligned} \tag{26}$$

$$\int_\Omega q(\nabla\cdot\boldsymbol{u})\,\mathrm{d}v = 0 \quad \forall q \in \mathscr{Q}, \tag{27}$$

$$\Phi_B\int_B\Big[\boldsymbol{w}'(\boldsymbol{s},t) - \boldsymbol{u}(\boldsymbol{x},t)\big|_{\boldsymbol{x}=\boldsymbol{\zeta}(\boldsymbol{s},t)}\Big]\cdot\boldsymbol{y}(\boldsymbol{s})\,\mathrm{d}V = 0 \quad \forall\boldsymbol{y}\in\mathscr{H}_Y, \tag{28}$$

where Φ_B is a constant with dimensions of mass over time divided by length cubed, i.e., dimensions such that, in 3D, the volume integral of the quantity $\Phi_B\boldsymbol{w}'$ has the same dimensions as a force.

We note that a key element of any fully variational formulation of immersed methods is (the variational formulation of) the equation enabling the tracking of the motion of the solid, here Eq. (28). In the discrete formulation, this relation is as general as the choice of the finite-dimensional functional subspaces approximating $\mathscr{V}$ and $\mathscr{Y}$ and it is key to the stability of the method.

The dual formulation of Eqs. (26)–(28) is as follows:

Problem 1 (Incompressible fluid, incompressible solid: dual formulation)**.** Given initial conditions $\boldsymbol{u}_0 \in \mathscr{V}$ and $\boldsymbol{w}_0 \in \mathscr{Y}$, for all $t \in (0,T)$ find $\boldsymbol{u}(\boldsymbol{x},t) \in \mathscr{V}$, $p(\boldsymbol{x},t) \in \mathscr{Q}$, and $\boldsymbol{w}(\boldsymbol{s},t) \in \mathscr{Y}$ such that

$$\begin{aligned}
&\mathcal{M}_{\alpha 1}\boldsymbol{u}' + \mathcal{N}_{\alpha 1}(\boldsymbol{u})\boldsymbol{u} + \mathcal{D}_{\alpha 1}\boldsymbol{u} + (\mathcal{B}_{\beta 1})^{\mathrm{T}}p \\
&\quad + \delta\mathcal{M}_{\alpha 1}(\boldsymbol{w})\boldsymbol{u}' + \delta\mathcal{N}_{\alpha 1}(\boldsymbol{w},\boldsymbol{w}',\boldsymbol{u})\boldsymbol{u} + \delta\mathcal{D}_{\alpha 1}(\boldsymbol{w})\boldsymbol{u} + \mathcal{S}_{\alpha\gamma}(\boldsymbol{w})\mathcal{A}_\gamma(\boldsymbol{w}) = \mathcal{F}_\alpha + \mathcal{G}_\alpha(\boldsymbol{w}),
\end{aligned} \tag{29}$$

$$\mathcal{B}_{\beta 1}\boldsymbol{u} = 0, \tag{30}$$

$$\mathcal{M}_{\gamma 3}\boldsymbol{w}' - \mathcal{M}_{\gamma 1}(\boldsymbol{w})\boldsymbol{u} = \boldsymbol{0}, \tag{31}$$

where, using the notation ${}_{V^*}\langle\psi,\phi\rangle_V$ to represent the duality product between V^* and V, we define the operator $\mathcal{M}_{\alpha 1}$ is defined as

$$\mathcal{M}_{\alpha 1} : \mathscr{H}_V \to \mathscr{V}^*, \quad {}_{\mathscr{V}^*}\langle\mathcal{M}_{\alpha 1}\boldsymbol{u},\boldsymbol{v}\rangle_{\mathscr{V}} := \int_\Omega \rho_{\mathrm{f}}\,\boldsymbol{u}\cdot\boldsymbol{v}\,\mathrm{d}v \quad \forall\boldsymbol{u}\in\mathscr{H}_V, \forall\boldsymbol{v}\in\mathscr{V}_0, \tag{32}$$

and where, for convenience, the explicit definition of the rest of the above operators is given in Eqs. (73)–(86) in the Appendix.

The subscript on an operators identify the domain and range of the operator. Specifically, the numbers 1, 2, and 3 identify the spaces $\mathscr{V}$, $\mathscr{Q}$, and $\mathscr{Y}$, respectively, while the Greek letter α, β, and γ identify the spaces $\mathscr{V}^*$, $\mathscr{Q}^*$, and $\mathscr{Y}^*$, respectively. Then, a Greek letter followed by a number identifies an operator whose domain is the space corresponding to the number, and whose co-domain is in the space corresponding to the Greek letter. So that, for example, $\mathcal{E}_{\alpha 2}$ and $\mathcal{E}_{\alpha 2}\, p$ denote a map ($\mathcal{E}_{\alpha 2}$) from $\mathscr{Q}$ into $\mathscr{V}^*$ and the action of this map ($\mathcal{E}_{\alpha 2}\, p \in \mathscr{V}^*$) on the field $p \in \mathscr{Q}$, respectively. If an operators has only one subscript, that subscript identifies the space containing the range of the operator.

Equation (29) represents the balance of linear momentum. The terms on the first line of this equation govern the Navier-Stokes flow of a fluid occupying the entire control volume Ω whereas the terms on the second line (to the left of the equal sign) describe the FSI component of the problem. Equation(30) expresses the incompressibility constraint. Finally, Eq. (31) expresses the velocity coupling between the fluid and the immersed domain.

Remark 2 (Eulerian vs. Lagrangian elastic operators). The treatment of the terms describing the effect of the elastic response of the solid on the fluid is crucial in the creation of a stable discrete formulation. The elastic response in question is represented by the last integral in Eq. (26). The latter is represented by the operator $\mathcal{A}_\alpha(\boldsymbol{w}, \boldsymbol{w})$ defined in Eq. (81). Heltai and Costanzo (2012) have shown that $\mathcal{A}_\alpha(\boldsymbol{w}, \boldsymbol{w})$ can be represented as follows:

$$\mathcal{A}_\alpha(\boldsymbol{w}, \boldsymbol{h}) = \mathcal{S}_{\alpha\gamma}(\boldsymbol{h})\mathcal{A}_\gamma(\boldsymbol{w}) \quad \text{where} \quad \mathcal{S}_{\alpha\gamma}(\boldsymbol{h}) = \mathcal{M}^{\mathrm{T}}_{\gamma 1}(\boldsymbol{h})\mathcal{M}^{-1}_{\gamma 3}, \tag{33}$$

where $\mathcal{S}_{\alpha\gamma}(\boldsymbol{h})\mathcal{A}_\gamma(\boldsymbol{w})$ and $\mathcal{M}^{\mathrm{T}}_{\gamma 1}(\boldsymbol{h})\mathcal{M}^{-1}_{\gamma 3}$ indicate the composition of the operators $\mathcal{S}_{\alpha\gamma}(\boldsymbol{h})$ and $\mathcal{A}_\gamma(\boldsymbol{w})$ and of the operators $\mathcal{M}^{\mathrm{T}}_{\gamma 1}(\boldsymbol{h})$ and $\mathcal{M}^{-1}_{\gamma 3}$, respectively. The operator $\mathcal{A}_\gamma(\boldsymbol{w})$ is the elasticity operator that arises naturally in Lagrangian variational formulations of nonlinear elastic problems. By contrast, we can view the operator $\mathcal{A}_\alpha(\boldsymbol{w}, \boldsymbol{h})$ as the Eulerian representation of the elasticity operator. Apart from theoretical niceties, it is important to observe that the elastic operator appears in Eq. (29) in the form $\mathcal{S}_{\alpha\gamma}(\boldsymbol{h})\mathcal{A}_\gamma(\boldsymbol{w})$. Heltai and Costanzo (2012) have shown that while there is no difference in writing $\mathcal{A}_\alpha(\boldsymbol{w}, \boldsymbol{w})$ or $\mathcal{S}_{\alpha\gamma}(\boldsymbol{h})\mathcal{A}_\gamma(\boldsymbol{w})$ in an abstract variational formulation, it is crucial to write the elastic operator as $\mathcal{S}_{\alpha\gamma}(\boldsymbol{h})\mathcal{A}_\gamma(\boldsymbol{w})$ when implementing this formulation in the discrete case because this form makes the discrete formulation stable.

3.3 Governing equations: compressible solid

When the solid is compressible, the contribution of p to the balance of linear momentum and the incompressibility constraint must be restricted to the domain $\Omega \setminus B_t$. Therefore, the weak problem is rewritten as follows:

$$\begin{aligned}
&\int_\Omega \rho_{\mathrm{f}}(\dot{\boldsymbol{u}} - \boldsymbol{b}) \cdot \boldsymbol{v}\, \mathrm{d}v - \int_\Omega p \operatorname{div} \boldsymbol{v}\, \mathrm{d}v + \int_\Omega \hat{\mathsf{T}}^v_{\mathrm{f}} \cdot \nabla_{\boldsymbol{x}} \boldsymbol{v}\, \mathrm{d}v - \int_{\partial\Omega_N} \boldsymbol{\tau}_g \cdot \boldsymbol{v}\, \mathrm{d}a \\
&\quad + \int_B \big\{[\rho_{\mathrm{s}_0}(\boldsymbol{s}) - \rho_{\mathrm{f}_0}][\dot{\boldsymbol{u}}(\boldsymbol{x}, t) - \boldsymbol{b}(\boldsymbol{x}, t)] \cdot \boldsymbol{v}(\boldsymbol{x})\big|_{\boldsymbol{x}=\boldsymbol{\zeta}(\boldsymbol{s},t)}\, \mathrm{d}V \\
&\quad\quad + \int_B J(\boldsymbol{s}, t) p(\boldsymbol{x}, t) \operatorname{div} \boldsymbol{v}(\boldsymbol{x})\big|_{\boldsymbol{x}=\boldsymbol{\zeta}(\boldsymbol{s},t)}\, \mathrm{d}V \\
&\quad\quad + \int_B J(\boldsymbol{s}, t)\big(\hat{\mathsf{T}}^v_{\mathrm{s}} - \hat{\mathsf{T}}^v_{\mathrm{f}}\big) \cdot \nabla_{\boldsymbol{x}} \boldsymbol{v}(\boldsymbol{x})\big|_{\boldsymbol{x}=\boldsymbol{\zeta}(\boldsymbol{s},t)}\, \mathrm{d}V \\
&\quad\quad\quad + \int_B \hat{\mathsf{P}}^e_{\mathrm{s}}\, \mathsf{F}^{\mathrm{T}}(\boldsymbol{s}, t) \cdot \nabla_{\boldsymbol{x}} \boldsymbol{v}(\boldsymbol{x})\big|_{\boldsymbol{x}=\boldsymbol{\zeta}(\boldsymbol{s},t)}\, \mathrm{d}V = 0 \quad \forall \boldsymbol{v} \in \mathscr{V}_0.
\end{aligned} \tag{34}$$

$$\int_\Omega q \operatorname{div} \boldsymbol{u} \, \mathrm{d}v - \int_{B_t} q \operatorname{div} \boldsymbol{u} \, \mathrm{d}v = 0, \tag{35}$$

$$\Phi_B \int_B \Big[\dot{\boldsymbol{w}}(\boldsymbol{s},t) - \boldsymbol{u}(\boldsymbol{x},t)\big|_{\boldsymbol{x}=\boldsymbol{\zeta}(\boldsymbol{s},t)} \Big] \cdot \boldsymbol{y}(\boldsymbol{s}) \, \mathrm{d}V = 0 \quad \forall \boldsymbol{y} \in \mathscr{H}_Y. \tag{36}$$

Equations (34)–(36) would allow us to determine a unique solution if the field p were restricted to the domain $\Omega \setminus B_t$. However, our numerical scheme still requires that p be defined everywhere in Ω. To formulate a problem admitting a unique solution for the field $p \in \mathscr{Q}$, we must sufficiently constraint the behavior of p over B_t. The strategy to enforce such a constraint is not unique. In some sense, p can be restricted to $\Omega \setminus B_t$ by requiring that $p = 0$ over B_t. Another, and perhaps more physically motivated, approach is to observe that, for a Newtonian fluid, p represents the mean normal stress in the fluid. Therefore, one may choose to constraint the field p in a such a way that it represents the mean normal stress everywhere in Ω. Since the solid is compressible, its mean normal stress is completely determined by the solid's stress constitutive response functions. Specifically, letting $\hat{p}_{\mathrm{s}}[\boldsymbol{u}, \boldsymbol{w}]$ denote the constitutive response function for the mean normal stress in the solid, we have

$$\hat{p}_{\mathrm{s}}[\boldsymbol{u}, \boldsymbol{w}] = -\frac{1}{\operatorname{tr} \mathsf{I}} \Big[\hat{\mathsf{T}}^v_{\mathrm{s}}[\boldsymbol{u}] \cdot \mathsf{I} + J^{-1}[\boldsymbol{w}] \hat{\mathsf{P}}^e_{\mathrm{s}}[\boldsymbol{w}] \cdot \mathsf{F}[\boldsymbol{w}] \Big]. \tag{37}$$

Therefore, in addition to enforcing Eq. (35), we can enforce the requirement that $p - \hat{p}_{\mathrm{s}}[\boldsymbol{u}, \boldsymbol{w}] = 0$ over B_t. With this in mind, we replace Eq. (35) with the following equation:

$$\begin{aligned} -\int_\Omega q \operatorname{div} \boldsymbol{u} \, \mathrm{d}v + \int_B J(\boldsymbol{s},t) q(\boldsymbol{x}) \operatorname{div} \boldsymbol{u}(\boldsymbol{x},t)\big|_{\boldsymbol{x}=\boldsymbol{\zeta}(\boldsymbol{s},t)} \, \mathrm{d}V \\ + \int_B c_1 J(\boldsymbol{s},t) \big[p(\boldsymbol{x},t) - c_2 \hat{p}_{\mathrm{s}}[\boldsymbol{u}, \boldsymbol{w}] \big] q(\boldsymbol{x})\big|_{\boldsymbol{x}=\boldsymbol{\zeta}(\boldsymbol{s},t)} \, \mathrm{d}V = 0 \quad \forall q \in \mathscr{Q}, \end{aligned} \tag{38}$$

where $c_1 > 0$ is a constant parameter with dimensions of length times mass over time, and where c_2 is a dimensionless constant that can take on only the values 0 or 1. For $c_2 = 0$, the last term on the left-hand side of Eq. (38) is a (weak) requirement that $p = 0$ over B_t, whereas for $c_2 = 1$, the field p is (weakly) constrained to be equal to the mean normal stress in the solid domain and therefore everywhere in Ω.

As was done in the incompressible case, we now reformulate our equations in terms of operators defined via duality. Most of the operators defined in the incompressible case appear in the formulation of the compressible solid case. Hence, we now define only those operators that did not appear in the previous case. Specifically, we define the following three operators:

These operators, along with those defined earlier, allow us to formally restate the overall problem described by Eqs. (34), (38), and (36) as follows:

Problem 2 (Incompressible fluid, compressible solid: dual formulation)**.** Given constant coefficients $c_1 > 0$ and $c_2 = 0 \vee 1$, and given initial conditions $\boldsymbol{u}_0 \in \mathscr{V}$ and $\boldsymbol{w}_0 \in \mathscr{Y}$, for all $t \in (0,T)$ find $\boldsymbol{u}(\boldsymbol{x},t) \in \mathscr{V}$, $p(\boldsymbol{x},t) \in \mathscr{Q}$, and $\boldsymbol{w}(\boldsymbol{s},t) \in \mathscr{Y}$ such that

$$\begin{aligned} &\mathcal{M}_{\alpha 1} \boldsymbol{u}' + \mathcal{N}_{\alpha 1}(\boldsymbol{u}) \boldsymbol{u} + \mathcal{D}_{\alpha 1} \boldsymbol{u} + \big[\mathcal{B}^{\mathrm{T}}_{\beta 1} + \delta \mathcal{B}^{\mathrm{T}}_{\beta 1}(\boldsymbol{w}) \big] p \\ &\quad + \delta \mathcal{M}_{\alpha 1}(\boldsymbol{w}) \boldsymbol{u}' + \delta \mathcal{N}_{\alpha 1}(\boldsymbol{w}, \boldsymbol{w}', \boldsymbol{u}) \boldsymbol{u} + \delta \mathcal{D}_{\alpha 1}(\boldsymbol{w}) \boldsymbol{u} + \mathcal{S}_{\alpha\gamma}(\boldsymbol{w}) \mathcal{A}_\gamma(\boldsymbol{w}) = \mathcal{F}_\alpha + \mathcal{G}_\alpha(\boldsymbol{w}), \end{aligned} \tag{39}$$

$$\big[\mathcal{B}_{\beta 1} + \delta \mathcal{B}_{\beta 1}(\boldsymbol{w}) \big] \boldsymbol{u} + c_1 \big[\delta \mathcal{P}_{\beta 2}(\boldsymbol{w}) p - c_2 \delta \mathcal{E}_\beta(\boldsymbol{u}, \boldsymbol{w}, \boldsymbol{w}) \big] = 0, \tag{40}$$

$$\mathcal{M}_{\gamma 3} \boldsymbol{w}' - \mathcal{M}_{\gamma 1}(\boldsymbol{w}) \boldsymbol{u} = \boldsymbol{0}, \tag{41}$$

where, for convenience, the definitions of the operators used in the above equations has been placed in the Appendix (see Eqs. (87)–(90) for the operator pertaining to the compressible formulation in particular).

Remark 3 (Complementarity of operators in $\mathscr{Q}^*$). In Eq. (40), the supports of the terms $\big[\mathcal{B}_{\beta 1} + \delta\mathcal{B}_{\beta 1}(\boldsymbol{w})\big]$ and $\big[\delta\mathcal{P}_{\beta 2}(\boldsymbol{w}) + c_2\delta\mathcal{E}_\beta(\boldsymbol{u},\boldsymbol{w},\boldsymbol{w})\big]$ are $\Omega \setminus B_t$ and B_t, respectively. That is, the supports of the terms in question are complementary subsets of Ω. Consequently, the terms $\big[\mathcal{B}_{\beta 1} + \delta\mathcal{B}_{\beta 1}(\boldsymbol{w})\big]$ and $\big[\delta\mathcal{P}_{\beta 2}(\boldsymbol{w}) + c_2\delta\mathcal{E}_\beta(\boldsymbol{u},\boldsymbol{w},\boldsymbol{w})\big]$ are equal to zero individually:

$$\big[\mathcal{B}_{\beta 1} + \delta\mathcal{B}_{\beta 1}(\boldsymbol{w})\big]\boldsymbol{u} = 0 \quad \text{and} \quad c_1\big[\delta\mathcal{P}_{\beta 2}(\boldsymbol{w})p - c_2\delta\mathcal{E}_\beta(\boldsymbol{u},\boldsymbol{w},\boldsymbol{w})\big] = 0. \tag{42}$$

This also implies that the constant c_1 in Eqs. (39) and the second of Eqs. (42) should not be interpreted as a penalization parameter but as a way to ensure that the equations are dimensionally correct.

Problems 1 and 2 can be formally presented in terms of the Hilbert space $\mathscr{Z} := \mathscr{V} \times \mathscr{Q} \times \mathscr{Y}$, and $\mathscr{Z}_0 := \mathscr{V}_0 \times \mathscr{Q} \times \mathscr{H}_Y$ with inner product given by the sum of the inner products of the generating spaces. Defining $\mathscr{Z} \ni \xi := [\boldsymbol{u}, p, \boldsymbol{w}]^{\mathrm{T}}$ and $\mathscr{Z}_0 \ni \psi := [\boldsymbol{v}, q, \boldsymbol{y}]^{\mathrm{T}}$, then Problems 1 and 2 can be compactly stated as

Problem 3 (Grouped dual formulation)**.** Given an initial condition $\xi_0 \in \mathscr{Z}$, for all $t \in (0, T)$ find $\xi(t) \in \mathscr{Z}$, such that

$$\langle \mathcal{F}(t, \xi, \xi'), \psi \rangle = 0, \quad \forall \psi \in \mathscr{Z}_0, \tag{43}$$

where the full expression of $\mathcal{F} : \mathscr{Z} \mapsto \mathscr{Z}_0^*$ is defined as in Problem 1 or Problem 2.

Remark 4 (Initial condition for the pressure). In Problem 3, an initial condition for the triple $\xi_0 = [\boldsymbol{u}_0, p_0, \boldsymbol{w}_0]^{\mathrm{T}}$ is required, just as a matter of compact representation of the problem. However, only the initial conditions $\boldsymbol{u}_0$ and $\boldsymbol{w}_0$ are used, since we have no time derivative for the pressure which is a Lagrange multiplier for the incompressible part of the problem, or completely determined by the solution in the compressible part.

Remark 5 (Energy estimates). Heltai and Costanzo (2012) have shown that the formulation presented thus far leads to energy estimates that that are formally identical to those of the continuous formulation.

4 Discrete Formulation

4.1 Spatial Discretization by finite elements

The abstract formulation introduced thus far is translated into a corresponding discrete formulation using standard FEM techniques. We introduce the decompositions Ω_h for Ω and B_h for B into (closed) cells K (triangles or quadrilaterals in 2D, and tetrahedra or hexahedra in 3D) such that the usual regularity assumptions are satisfied:

1. $\overline{\Omega} = \cup\{K \in \Omega_h\}$, and $\overline{B} = \cup\{K \in B_h\}$;
2. Any two cells K, K' only intersect in common faces, edges, or vertices;
3. The decomposition Ω_h matches the decomposition $\partial\Omega = \partial\Omega_D \cup \partial\Omega_N$.

On the decompositions Ω_h and B_h, we consider the finite dimensional subspaces $\mathscr{V}_h \subset \mathscr{V}$, $\mathscr{Q}_h \subset \mathscr{Q}$, and $\mathscr{Y}_h \subset \mathscr{Y}$ defined as

$$\mathscr{V}_h := \Big\{ \boldsymbol{u}_h \in \mathscr{V} \;\Big|\; \boldsymbol{u}_{h|K} \in \mathcal{P}_V(K),\, K \in \Omega_h \Big\} \equiv \operatorname{span}\{\boldsymbol{v}_h^i\}_{i=1}^{N_V} \tag{44}$$

$$\mathscr{Q}_h := \Big\{ p_h \in \mathscr{Q} \;\big|\; p_{h|K} \;\in \mathcal{P}_Q(K),\, K \in \Omega_h \Big\} \equiv \operatorname{span}\{q_h^i\}_{i=1}^{N_Q} \tag{45}$$

$$\mathscr{Y}_h := \Big\{ \boldsymbol{w}_h \in \mathscr{Y} \;\big|\; \boldsymbol{w}_{h|K} \in \mathcal{P}_Y(K),\, K \in B_h \Big\} \equiv \operatorname{span}\{\boldsymbol{y}_h^i\}_{i=1}^{N_Y}, \tag{46}$$

where $\mathcal{P}_V(K)$, $\mathcal{P}_Q(K)$ and $\mathcal{P}_Y(K)$ are polynomial spaces of degree r_V, r_Q and r_Y respectively on the cells K, and N_V, N_Q and N_Y are the dimensions of each finite dimensional space. The finite dimensional spaces $\mathscr{V}_h$ and $\mathscr{Y}_h$ are included in the pivot spaces $\mathscr{H}_V$ and $\mathscr{H}_Y$, respectively, which allow us to use only one discrete space for both $\boldsymbol{u}$ and $\boldsymbol{u}'$ and one for $\boldsymbol{w}$ and $\boldsymbol{w}'$. Also, we chose the pair $\mathscr{V}_h$ and $\mathscr{Q}_h$ so as to satisfy the inf-sup condition for existence, uniqueness, and stability of the approximate solution pertaining to the Navier-Stokes component of the problem (see, e.g., Brezzi and Fortin, 1991).

The discrete versions of Problems 1 and 2 requires the introduction of additional notation. Given a discrete space, say, $\mathscr{V}_h$, one of its elements $\boldsymbol{u}_h$ is identified by the column vector of time dependent coefficients $u_h^j(t)$, $j = 1, \ldots, N_V$, such that $\boldsymbol{u}_h(\boldsymbol{x}, t) = \sum u_h^j(t) \boldsymbol{v}_h^j(\boldsymbol{x})$, where $\boldsymbol{v}_h^j$ is the j^{th} base element of $\mathscr{V}_h$. We write $M_{\alpha 1}\boldsymbol{u}_h$ to mean the multiplication of the column vector $\boldsymbol{u}_h$ by the matrix whose elements $M_{\alpha 1}^{ij}$, where $M_{\alpha 1}^{ij} := {}_{\mathscr{V}^*}\langle \mathcal{M}_{\alpha 1} \boldsymbol{v}_h^j, \boldsymbol{v}_h^i \rangle_{\mathscr{V}}$. and where the operator in angle brackets is the one defined earlier. A similar notation is adopted int he matrix representation of the operators appearing in the duel formulation.

Given a choice of Ω_h and B_h and corresponding finite dimensional spaces $\mathscr{V}_h$, $\mathscr{Q}_h$, and $\mathscr{Y}_h$, we reformulate Problem 1 as follows:

Problem 4. Given $\boldsymbol{u}_0 \in \mathscr{V}_h$, $\boldsymbol{w}_0 \in \mathscr{Y}_h$, for all $t \in (0, T)$, find $\boldsymbol{u}_h(t) \in \mathscr{V}_h$, $p_h(t) \in \mathscr{Q}_h$, and $\boldsymbol{w}_h(t) \in \mathscr{Y}_h$ such that

$$\begin{aligned} M_{\alpha 1}\boldsymbol{u}_h' + N_{\alpha 1}(\boldsymbol{u}_h)\boldsymbol{u}_h + D_{\alpha 1}\boldsymbol{u}_h + (B_{\beta 1})^{\mathrm{T}} p_h \\ + \delta M_{\alpha 1}(\boldsymbol{w}_h)\boldsymbol{u}_h' + \delta N_{\alpha 1}(\boldsymbol{w}_h, \boldsymbol{w}_h', \boldsymbol{u}_h)\boldsymbol{u}_h \\ + \delta D_{\alpha 1}(\boldsymbol{w}_h)\boldsymbol{u}_h + S_{\alpha\gamma}(\boldsymbol{w}_h) A_\gamma(\boldsymbol{w}_h) = F_\alpha + G_\alpha(\boldsymbol{w}_h), \end{aligned} \tag{47}$$

$$B_{\beta 1}\boldsymbol{u}_h = 0, \tag{48}$$

$$M_{\gamma 3}\boldsymbol{w}_h' - M_{\gamma 1}(\boldsymbol{w}_h)\boldsymbol{u}_h = \boldsymbol{0}, \tag{49}$$

where $\boldsymbol{u}_h'(\boldsymbol{x}, t) = \sum [u_h^j(t)]' \boldsymbol{v}_h^j(\boldsymbol{x})$ and $\boldsymbol{w}_h'(\boldsymbol{s}, t) = \sum [w_h^j(t)]' \boldsymbol{y}_h^j(\boldsymbol{s})$, and where the prime denotes ordinary differentiation with respect to time.

Similarly, for Problem 2 we have:

Problem 5. Given constant coefficients $c_1 > 0$ and $c_2 = 0 \vee 1$, and given initial conditions $\boldsymbol{u}_0 \in \mathscr{V}_h$ and $\boldsymbol{w}_0 \in \mathscr{Y}_h$, for all $t \in (0, T)$ find $\boldsymbol{u}_h(\boldsymbol{x}, t) \in \mathscr{V}_h$, $p_h(\boldsymbol{x}, t) \in \mathscr{Q}_h$, and $\boldsymbol{w}_h(\boldsymbol{s}, t) \in \mathscr{Y}_h$ such that

$$\begin{aligned} M_{\alpha 1}\boldsymbol{u}_h' + N_{\alpha 1}(\boldsymbol{u}_h)\boldsymbol{u}_h + D_{\alpha 1}\boldsymbol{u}_h + \big[B_{\beta 1} + \delta B_{\beta 1}(\boldsymbol{w}_h)\big]^{\mathrm{T}} p_h \\ + \delta M_{\alpha 1}(\boldsymbol{w}_h)\boldsymbol{u}_h' + \delta N_{\alpha 1}(\boldsymbol{w}_h, \boldsymbol{w}_h', \boldsymbol{u}_h)\boldsymbol{u}_h \\ + \delta D_{\alpha 1}(\boldsymbol{w}_h)\boldsymbol{u}_h + S_{\alpha\gamma}(\boldsymbol{w}_h) A_\gamma(\boldsymbol{w}_h) = F_\alpha + G_\alpha(\boldsymbol{w}_h), \end{aligned} \tag{50}$$

$$\big[B_{\beta 1} + \delta B_{\beta 1}(\boldsymbol{w}_h)\big]\boldsymbol{u}_h + c_1 \big[\delta P_{\beta 2}(\boldsymbol{w}_h) p_h - c_2 \delta E_{\beta 2}(\boldsymbol{u}_h, \boldsymbol{w}_h, \boldsymbol{w}_h)\big] = 0, \tag{51}$$

$$M_{\gamma 3}\boldsymbol{w}_h' - M_{\gamma 1}(\boldsymbol{w}_h)\boldsymbol{u}_h = \boldsymbol{0}, \tag{52}$$

where $\boldsymbol{u}_h'(\boldsymbol{x}, t) = \sum [u_h^j(t)]' \boldsymbol{v}_h^j(\boldsymbol{x})$ and $\boldsymbol{w}_h'(\boldsymbol{s}, t) = \sum [w_h^j(t)]' \boldsymbol{y}_h^j(\boldsymbol{s})$, and where the prime denotes ordinary differentiation with respect to time.

In compact notation, Problems 4 and 5 can be cast as semi-discrete problems in the space $\mathscr{Z} \supset \mathscr{Z}_h := \mathscr{V}_h \times \mathscr{Q}_h \times \mathscr{Y}_h$ as

Problem 6. Given an initial condition $\xi_0 \in \mathscr{Z}_h$, for all $t \in (0,T)$ find $\xi_h(t) \in \mathscr{Z}_h$, such that

$$F(t, \xi_h, \xi_h') = 0, \tag{53}$$

where

$$F^i(t, \xi_h, \xi_h') := \langle \mathcal{F}(t, \xi_h, \xi_h'), \psi_h^i \rangle, \quad i = 0, \ldots, N_V + N_Q + N_Y, \tag{54}$$

and $\mathcal{F}$ has the same meaning as in Eq. (43), with ψ_h^i being the basis function for the spaces $\mathscr{V}_h$, $\mathscr{Q}_h$, or $\mathscr{Y}_h$ corresponding to the given value of i.

Remark 6 (Semi-discrete strong consistency). Heltai and Costanzo (2012) have shown that the discrete formulations in Problem 4 and Problem 5 are strongly consistent.

Remark 7 (Spread operator). The only operator that couples *directly* the Eulerian and the Lagrangian framework is $\mathcal{M}_{\gamma 1}(\boldsymbol{w})$. In the IBM literature, the adjoint of $\mathcal{M}_{\gamma 1}(\boldsymbol{w})$ is also known as the *spread* operator, because of its role in distributing the forces due to the elastic deformation of the immersed domain to the underlying fluid domain.

4.2 Variational velocity coupling

The implementation of operator with support over Ω is common in FEM approaches to the Navier-Stokes equation. What is less common in the practical implementation of operators defined over B involving the evaluation of fields supported over Ω_h. This implementation has been discussed in detail by Heltai et al. (2012). Here we outline the basic features of the implementation. For simplicity, we describe the treatment of one such operators, namely, the matrix $M_{\gamma 1}(\boldsymbol{w})$ (corresponding to the operator defined in Eq. (83)) which is responsible for a successful coupling of velocities between the fluid and the solid domain.

Recall that the ij element of $M_{\gamma 1}(\boldsymbol{w}_h)$ is

$$\begin{aligned} M_{\gamma 1}^{ij}(\boldsymbol{w}_h) &= {}_{\mathscr{H}_Y^*}\big\langle \mathcal{M}_{\gamma 1}(\boldsymbol{w}_h)\boldsymbol{v}_h^j, \boldsymbol{y}_h^i \big\rangle_{\mathscr{H}_Y} \\ &= \Phi_B \int_B \boldsymbol{v}_h^j(\boldsymbol{x})\big|_{\boldsymbol{x}=\boldsymbol{s}+\boldsymbol{w}_h(\boldsymbol{s},t)} \cdot \boldsymbol{y}_h^i(\boldsymbol{s})\,\mathrm{d}V. \end{aligned} \tag{55}$$

The computation of the integral in Eq. (55) is done by summing the contributions due to each cell K in B_h via a quadrature rules with N_Q points. The functions $\boldsymbol{y}_h^i(\boldsymbol{s})$ have support over B_h, whereas the functions $\boldsymbol{v}_h^j(\boldsymbol{x})$ (with $\boldsymbol{x} = \boldsymbol{s} + \boldsymbol{w}_h(\boldsymbol{s}, t)$) have support on Ω_h. Hence, we first we determine the position of the quadrature points of the solid element, both relative to the reference unit element and relative to the underlying global coordinate system through the mappings:

$$\boldsymbol{s}_K : \hat{K} := [0,1]^d \mapsto K \in B_h, \tag{56}$$

$$I + \boldsymbol{w}_h : K \mapsto \text{solid cell}. \tag{57}$$

These global coordinates are passed to an algorithm that finds the fluid cells in Ω_h containing the points in question. The outcome of this operation is sketched in Fig. 2 where we show the deformed configuration of a cell of B_h straddling four cells of Ω_h denoted fluid cells A–D. The quadrature points over the solid cell are represented by the filled circles.

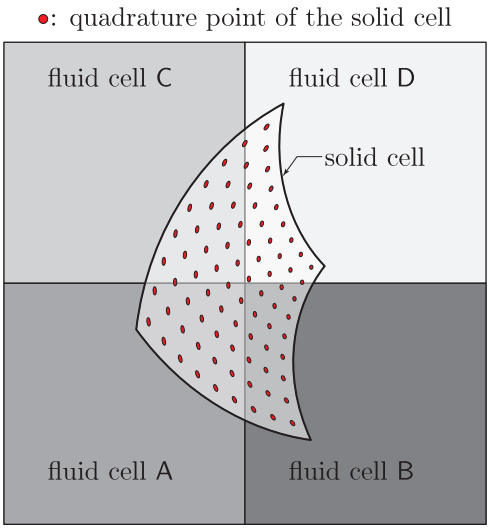

Figure 2: Cells denote as A–D represent a four-cell patch of the triangulation of the fluid domain. The cell denoted as "solid cell" represents a cell of the triangulation of the immersed solid domain that is contained in the union of cells A–D of the fluid domain. The filled dots represent the quadrature points of the quadrature rule adopted to carry out integration over the cells of the immersed domain.

4.3 Time discretization

Equation (53) represents a system of nonlinear differential algebraic equations (DAE), which we solve using a Newton iteration. In the code accompanying this paper, the time derivative ξ' is approximated very simply via an implicit-Euler scheme:

$$\xi'_n = h^{-1}\big(\xi_n - \xi_{n-1}\big), \tag{58}$$

where ξ_n and ξ'_n are the computed approximations to $\xi(t_n)$ and $\xi'(t_n)$, respectively, and the step size $h = t_n - t_{n-1}$ is kept constant throughout the computation. Although not second order accurate, this time stepping scheme is asymptotically stable.

The application of the implicit-Euler scheme in Eq. (58) to the DAE system in Eq. (53) results in a nonlinear algebraic system to be solved at each step:

$$G(\xi_n) := F\Big(t_n, \xi_n, h^{-1}\big(\xi_n - \xi_{n-1}\big)\Big) = 0. \tag{59}$$

The nonlinear system in Eq. (59) is solved via Newton iterations. This leads to a linear system for each Newton correction, of the form

$$J[\xi_{n,m+1} - \xi_{n,m}] = -G(\xi_{n,m}), \tag{60}$$

where $\xi_{n,m}$ is the mth approximation to ξ_m. Here J is some approximation to the system's Jacobian

$$J = \frac{\partial G}{\partial \xi} = \frac{\partial F}{\partial \xi} + \alpha \frac{\partial F}{\partial \xi'}, \tag{61}$$

where $\alpha = 1/h$. In our finite element implementation, we assemble the residual $G(\xi_{n,m})$ at each Newton correction. The implementation of the residual vector is based on the formulation presented in Problem 4. However, this formulation makes the determination of the corresponding

Jacobian rather involved due to the structure of the operator $\mathcal{S}_{\alpha\gamma}(\boldsymbol{w})$ (see Eq. (33)). Hence, we have implemented a Newton-Raphson iteration based on an approximate Jacobian. With reference to Eq. (33), the Jacobian we assemble is the exact Jacobian of a formulation in which the operator product $\mathcal{S}_{\alpha\gamma}(\boldsymbol{w})\mathcal{A}_{\gamma}(\boldsymbol{w})$ is replaced by the operator $\mathcal{A}_{\alpha}(\boldsymbol{w},\boldsymbol{h})$. The final system is solved using the direct solver provided by the `UMFPACK` package (see Davis, 2004).

5 Numerics

To the authors' knowledge, immersed methods have not been subject to validation in the same way as ALE methods have (cf., e.g., Turek and Hron, 2006). In this paper we present results that, in our opinion, validate the method and its effectiveness in solving FSI problems. We point out that in previous works concerning the use of fully variational approaches to the immersed finite element method, the immersed body was assumed to be viscoelastic (with a linear viscous component formally similar to that of the fluid) (cf. Boffi et al., 2008; Heltai, 2006, 2008; Heltai and Costanzo, 2012). In this paper, we present for the first time results in which the immersed body is compressible and purely hyperelastic. Furthermore, we consider cases in which the immersed solid and the fluid have different densities as well as dynamic viscosities (when the solid is assumed to have a linear viscous component to its stress response). We want to emphasize that in all simulations, even those with a compressible elastic body, the fluid is always modeled as incompressible, as opposed to nearly incompressible.

5.1 Discretization

The approximation spaces we used in our simulations for the approximations of the velocity field $\boldsymbol{u}_h$ and of the displacement field $\boldsymbol{w}_h$ are the piecewise bi-quadratic spaces of continuous vector functions over Ω and over B, respectively, which we will denote by $\mathcal{Q}_0^2$ space.* For the pressure field p, in some cases we have used the piecewise continuous bi-linear space $\mathcal{Q}_0^1$ and in other cases the piecewise discontinuous linear space $\mathcal{P}_{-1}^1$ over Ω. Both the $\mathcal{Q}_0^2$-$|\mathcal{Q}_0^1$ and the $\mathcal{Q}_0^2|\mathcal{P}_{-1}^1$ pairs of spaces are known to satisfy the inf-sup condition for the approximation of the Navier-Stokes part of our equations (see, e.g., Brezzi and Fortin, 1991). The choice of the space $\mathcal{Q}_0^2$ for the displacement variable $\boldsymbol{w}_h$ is a natural choice, given the underlying velocity field $\boldsymbol{u}_h$. With this choice of spaces, Eqs. (52) and (49) can be satisfied exactly when the solid and the fluid meshes are matching.

5.2 Results for Incompressible Immersed Solids

5.2.1 Static equilibrium of an annular solid comprising circumferential fibers and immersed in a stationary fluid

This numerical test is motivated by the ones presented in Boffi et al. (2008); Griffith and Luo (2012). The objective of this test is to compute the equilibrium state of an initially undeformed thick annular cylinder submerged in a stationary incompressible fluid that is contained in a rigid prismatic box having a square cross-section. As such, this is an example pertaining to Problem 1 and its discrete counterpart Problem 4.

Our simulation is two-dimensional and comprises an annular solid with inner radius R and thickness w, and filled with a stationary fluid that is contained in a square box of edge length l (see

*In general, we denote by $\mathcal{Q}_c^p$ the space of piecewise polynomials consisting of tensor products of polynomials of order p and with global continuity degree c. We denote by $\mathcal{P}_c^p$ the spaces of piecewise polynomials of maximum order p and continuity degree c. In all cases a subscript $c = -1$ denotes discontinuous spaces.

Fig. 3). The reference and deformed configurations can be described via polar coordinate systems with origins at the center of the annulus and whose unit vectors are given by $(\hat{\boldsymbol{u}}_R, \hat{\boldsymbol{u}}_\Theta)$ and $(\hat{\boldsymbol{u}}_r, \hat{\boldsymbol{u}}_\theta)$, respectively. This ring is subjected to the hydrostatic pressure of the fluid p_i and p_o at its inner and

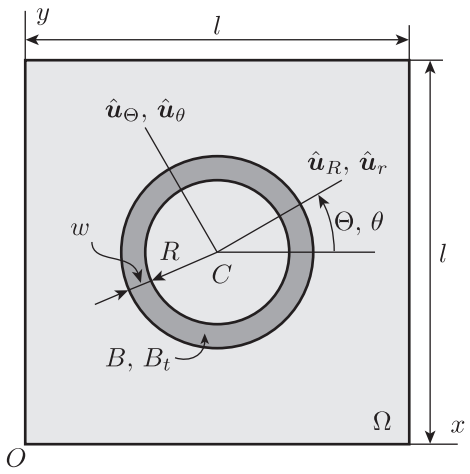

Figure 3: The reference and deformed configurations of a ring immersed in a square box filled with stationary fluid.

outer walls, respectively. Negligible body forces act on the system and there is no inflow or outflow of fluid across the walls of the box. Since both the solid and the fluid are incompressible, neither the annulus nor the fluid will move and the problem reduces to determining the Lagrange multiplier field p. The elastic behavior of the ring is governed by a continuous distribution of concentric fibers lying in the circumferential direction. The first Piola-Kirchhoff and the Cauchy stress tensors are then given by, respectively,

$$\hat{\mathsf{P}} = -p_{\mathrm{s}}\mathsf{F}^{-T} + \mu^e \mathsf{F}\hat{\boldsymbol{u}}_\Theta \otimes \hat{\boldsymbol{u}}_\Theta \quad \text{and} \quad \hat{\mathsf{T}}_{\mathrm{s}} = -p_{\mathrm{s}}\mathsf{I} + \mu^e \hat{\boldsymbol{u}}_\theta \otimes \hat{\boldsymbol{u}}_\theta, \tag{62}$$

where μ^e is a constant, p_s is the Lagrange multiplier that enforces incompressibility of the ring and $\hat{\boldsymbol{u}}_\theta = \hat{\boldsymbol{u}}_\Theta$ (since deformed and reference configurations coincide). Recall that in the proposed immersed FEM we have a single field p representing the Lagrange multiplier everywhere, whether in the fluid or in the solid. Therefore, we have $p = p_{\mathrm{s}}$ in the solid. With this in mind, we observe that the equilibrium stress state in the fluid is purely hydrostatic. Furthermore, since the boundary conditions on $\partial\Omega$ of of homogeneous Dirichlet type, the solution for the Lagrange multiplier p over Ω is not unique. We remove the non uniqueness by enforcing a zero average constraint on the field p. Then in can be shown (cf. Heltai et al., 2012) that the solution for the field p is as follows:

$$p = \begin{cases} p_o = -\frac{\pi\mu^e}{2l^2}\left((R+w)^2 - R^2\right) & \text{for} \quad R + w \le r, \\ p_s = \mu^e \ln(\frac{R+w}{r}) - \frac{\pi\mu^e}{2l^2}\left((R+w)^2 - R^2\right) & \text{for} \quad R < r < R + w, \\ p_i = \mu^e \ln(1 + \frac{w}{R}) - \frac{\pi\mu^e}{2l^2}\left((R+w)^2 - R^2\right) & \text{for} \quad r \le R, \end{cases} \tag{63}$$

with velocity of fluid $\boldsymbol{u} = \boldsymbol{0}$ and the displacement of the solid $\boldsymbol{w} = \boldsymbol{0}$. Note that Eq. (63) is different from Eq. (69) of Boffi et al. (2008), where p varies linearly with r (we believe this to be in error).

For all our numerical simulations we have used $R = 0.25\,\mathrm{m}$, $w = 0.062{,}50\,\mathrm{m}$, $l = 1.0\,\mathrm{m}$ and $\mu^e = 1\,\mathrm{Pa}$ and for these values we obtain $p_i = 0.167{,}92\,\mathrm{Pa}$ and $p_o = -0.055{,}22\,\mathrm{Pa}$ using Eq. (63).

We have used $\rho = 1.0\,\mathrm{kg/m^3}$, dynamic viscosity $\mu = 1.0\,\mathrm{Pa{\cdot}s}$, and time step size $h = 1 \times 10^{-3}\,\mathrm{s}$ in our tests. For all our numerical tests we have used $\mathcal{Q}_0^2$ elements to represent $\boldsymbol{w}$ of the solid, whereas we have used (i) $\mathcal{Q}_0^2|\mathcal{P}_{-1}^1$ elements, and (ii) $\mathcal{Q}_0^2|\mathcal{Q}_0^1$ elements to represent $\boldsymbol{v}$ and p over the control volume. We present a sample profile of p over the entire control volume and its variation along different values of y, after one time step, in Fig. 4 and Fig. 5 for $\mathcal{Q}_0^2|\mathcal{P}_{-1}^1$ and $\mathcal{Q}_0^2|\mathcal{Q}_0^1$ elements, respectively.

The order the convergence rate (see, Tables 1 and 2 for $\mathcal{Q}_0^2|\mathcal{P}_{-1}^1$ and $\mathcal{Q}_0^2|\mathcal{Q}_0^1$ elements, respectively) is 2.5 for the L^2 norm of the velocity, 1.5 for the H^1 norm of the velocity and 1.5 for the L^2 norm of the pressure which matches the rates presented in Boffi et al. (2008). In all these numerical tests we have used 1,856 cells with 15,776 DoFs for the solid.

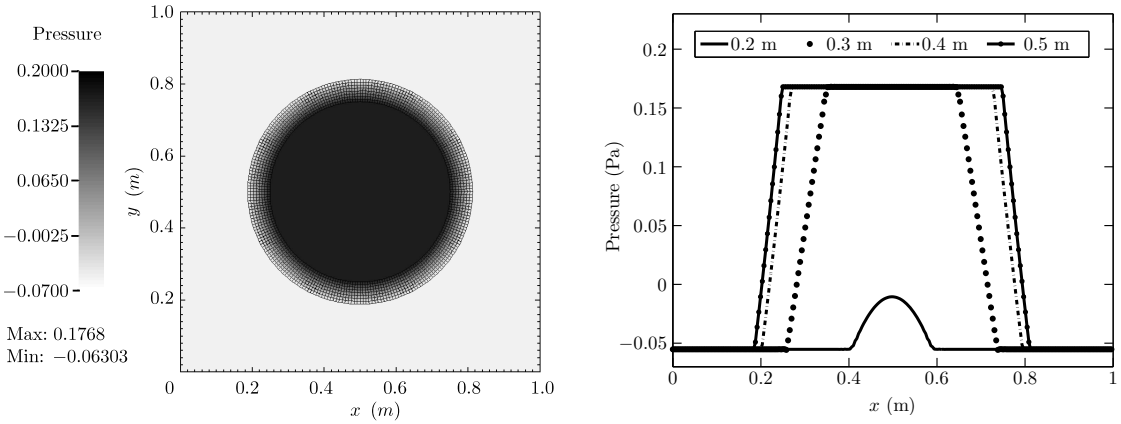

(a) Over the entire domain

(b) At different values of y

Figure 4: The values of p after one time step when using $\mathcal{P}_{-1}^1$ elements for p.

Table 1: Error convergence rate obtained when using $\mathcal{P}_{-1}^1$ element for p after one time step.

No. of cells	No. of DoFs	$\|\mathbf{u}_h - \mathbf{u}\|_0$		$\|\mathbf{u}_h - \mathbf{u}\|_1$		$\|p_h - p\|_0$	
256	2,946	2.00605e-05	-	1.95854e-03	-	6.71603e-03	-
1,024	11,522	3.69389e-06	2.44	7.44696e-04	1.40	2.47476e-03	1.44
4,096	45,570	5.76710e-07	2.68	2.25134e-04	1.73	8.74728e-04	1.50
16,384	181,250	1.06127e-07	2.44	8.24609e-05	1.45	3.14028e-04	1.48

5.2.2 Disk entrained in a lid-driven cavity flow

We test the volume conservation of our numerical method by measuring the change in the area of a disk that is entrained in a lid-driven cavity flow of an incompressible, linearly viscous fluid. This is another example pertaining to Problem 1 and its discrete counterpart Problem 4. This test is motivated by similar ones presented in Griffith and Luo (2012); Wang and Zhang (2010). Referring to Fig. 6, the disk has a radius $R = 0.2\,\mathrm{m}$ and its center C is initially positioned at $x = 0.6\,\mathrm{m}$ and $y = 0.5\,\mathrm{m}$ in the square cavity whose each edge has the length $l = 1.0\,\mathrm{m}$. Body forces on the system

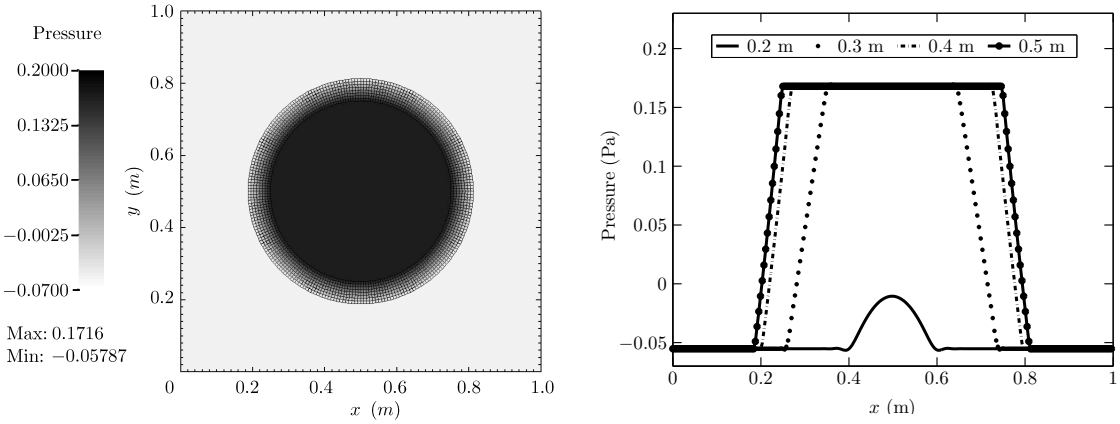

(a) Over the entire domain

(b) At different values of y

Figure 5: The values of p after one time step when using $\mathcal{Q}_0^1$ elements for p.

Table 2: Error convergence rate obtained when using $\mathcal{Q}_0^1$ element for p after one time step.

No. of cells	No. of DoFs	$\|\mathbf{u}_h - \mathbf{u}\|_0$		$\|\mathbf{u}_h - \mathbf{u}\|_1$		$\|p_h - p\|_0$	
256	2,467	4.36912e-05	-	2.79237e-03	-	7.39310e-03	-
1,024	9,539	6.14959e-06	2.83	9.02397e-04	1.63	2.42394e-03	1.61
4,096	37,507	1.28224e-06	2.26	3.49329e-04	1.37	9.10608e-04	1.41
16,384	148,739	2.33819e-07	2.46	1.25626e-04	1.48	3.27256e-04	1.48

are negligible. The constitutive elastic response of the disk is as follows:

$$\hat{\mathsf{P}} = -p_{\mathrm{s}}\mathsf{I} + \mu^e \mathsf{F}. \tag{64}$$

We have used the following parameters: $\rho = 1.0\,\mathrm{kg/m^3}$, dynamic viscosity $\mu = 0.01\,\mathrm{Pa{\cdot}s}$, shear modulus $\mu^e = 0.1\,\mathrm{Pa}$ and $U = 1.0\,\mathrm{m/s}$. For our numerical simulations we have used $\mathcal{Q}_0^2$ elements to represent $\boldsymbol{w}$ of the disk whereas we have used $\mathcal{Q}_0^2|\mathcal{P}_{-1}^1$ element for the fluid. The disk is represented using 320 cells with 2,626 DoFs and the control volume has 4,096 cells and 45,570 DoFs. The time step size $h = 1 \times 10^{-2}\,\mathrm{s}$. We consider the time interval $0 < t \leq 8\,\mathrm{s}$ during which the disk is lifted from its initial position along the left vertical wall, drawn along underneath the lid and finally dragged downwards along the right vertical wall of the cavity (see Fig. 7). As the disk trails beneath the lid, it experiences large shearing deformations (see Fig. 8). Ideally the disk should have retained its original area over the course of time because the incompressibility of the media and the nature of the motion require that the disk change its shape only and not its volume. However, as shown in Fig. 9, from our numerical scheme we obtain an area change of the disk of about 4% (cf. Griffith, 2012).

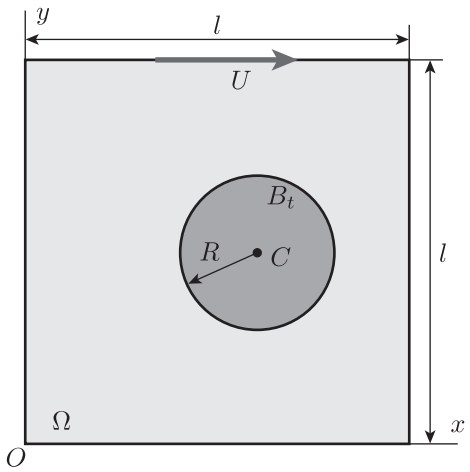

Figure 6: The initial configuration of an immersed disk entrained in a flow in a square cavity whose lid is driven with a velocity U towards the right.

5.2.3 Cylinder Falling in Viscous Fluid

In the previous examples, the fluid and the solid had the same density and dynamic viscosity. Here we modify this choice while considering again an example of Problem 1 and its discrete counterpart Problem 4. We present numerical tests partly inspired by those in Zhang and Gay (2007); Zhang et al. (2004b) meant to simulate experiments performed using a falling sphere viscometer. Specifically, we investigate the effect of changing the density of the solid and the viscosity of the fluid on the terminal velocity of the solid. Also, we estimate the drag coefficient of the falling object and discuss how the results depend on the mesh refinement.

The modeling of a cylinder sinking in a viscous fluid was first developed for the case of a rigid cylinder of length L and radius R released from rest in a quiescent unbounded fluid. We use the suffix ∞ to distinguish the results for this ideal case from those concerning a cylinder sinking in a bounded fluid medium. The longitudinal axis of the cylinder is assumed to be perpendicular to

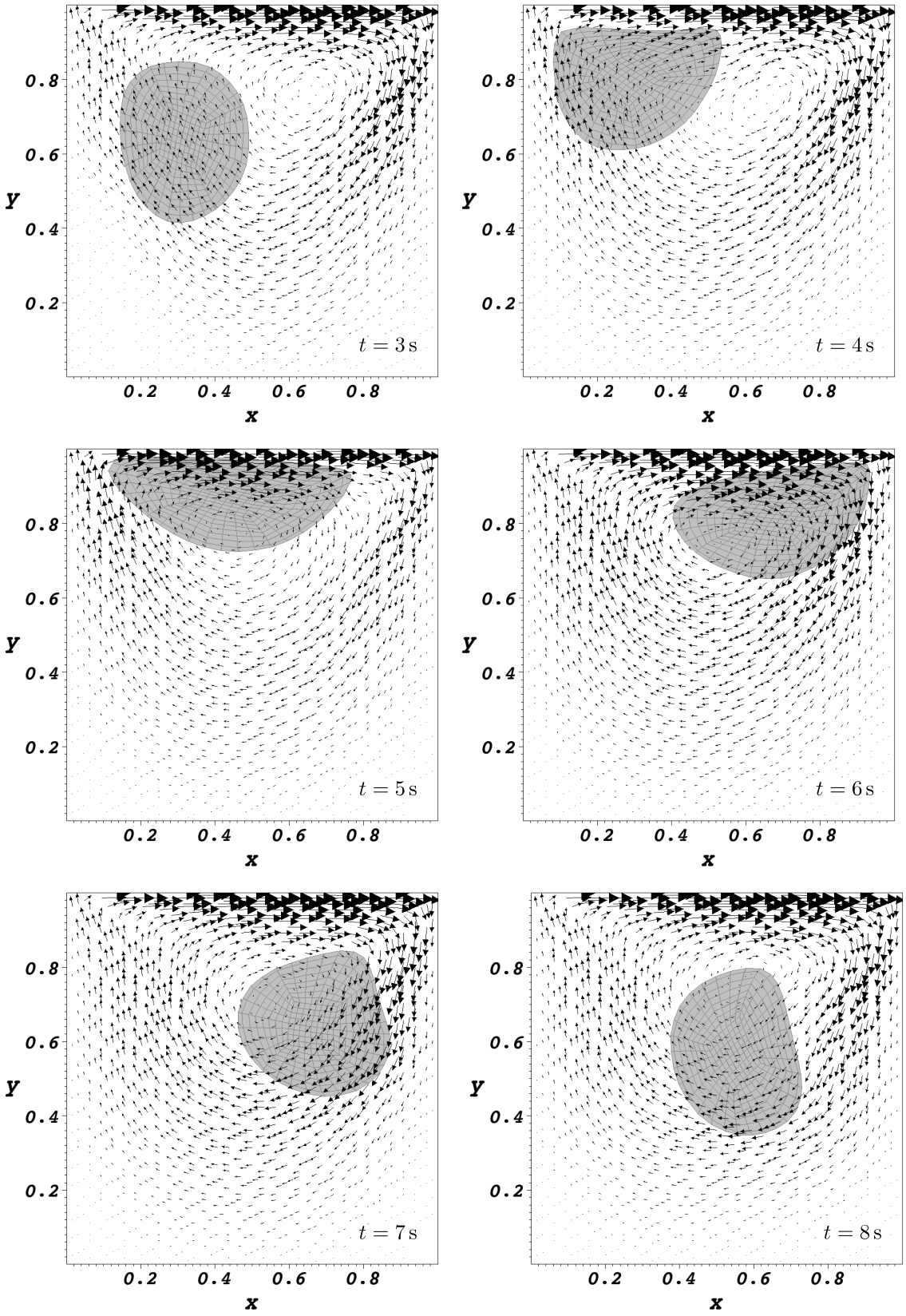

Figure 7: The motion of a disk at different instants of time.

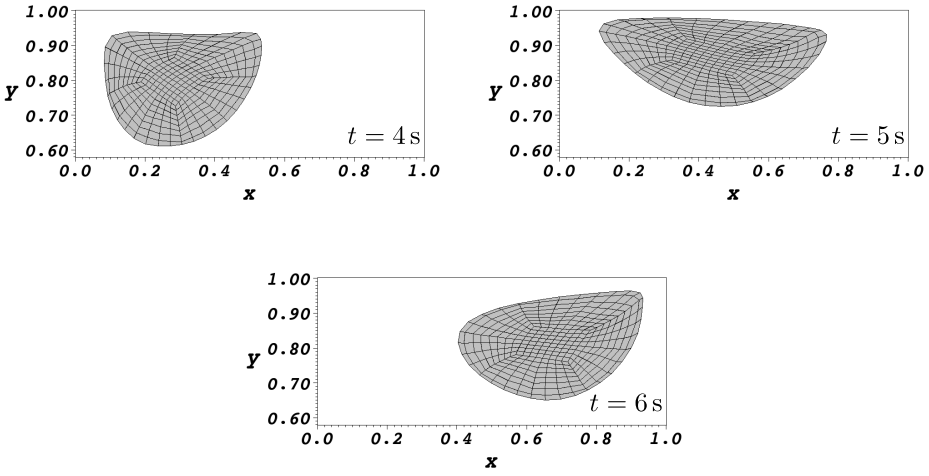

Figure 8: Enlarged view of the disk depicting its shape and location at various instants of time.

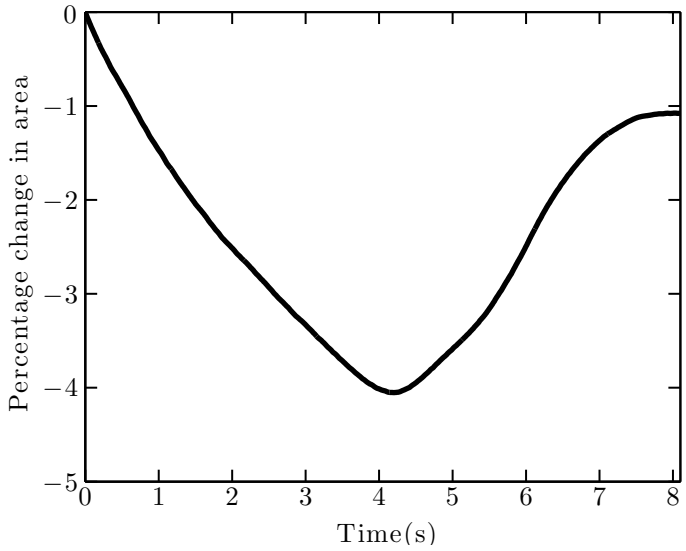

Figure 9: The percentage change in the area of the disk over time.

the direction of gravity and to remain so. If the density of the cylinder and the fluid are the same, the cylinder will remain neutrally buoyant. If $\rho_s > \rho_f$, the weight of the cylinder will exceed the buoyancy force and will descend through the fluid with a velocity $u_{Cy\infty}$, parallel to the gravitational field, under the action of a net force with magnitude $F_W = (\rho_s - \rho_f)\, ALg$, where $A = \pi R^2$ is the cross-sectional area of the cylinder and g is the acceleration due to gravity. Under creeping flow conditions, $F_{D\infty} = -\mu_f\, c\, u_{Cy\infty}$, where c is a constant. For a long cylinder, $c = 4\pi L/[\ln(2E) + 1 - \kappa]$ (Clift et al., 1978) where $E = L/(2R)$ is the aspect ratio for the cylinder and κ is a constant whose values have been determined to be 0.72 and 0.80685 by different researchers. When $F_{D\infty}$ balances F_W, the cylinder reaches terminal velocity $U_{t\infty} = [(\rho_s - \rho_f)ALg]/(\mu_f\, c)$. In real experiments, the fluid volume is finite and the resulting drag force F_D is larger than $F_{D\infty}$ due to effect of the confining walls. With this in mind, following Brenner (1962), we have that $F_{D\infty}$ at some speed u_∞ is related to F_D at the same speed u_∞ as $F_D = F_{D\infty}/\alpha$, where $0 < \alpha < 1$ is a constant for a given experimental setup. Moreover, Jayaweera and Mason (1965) show that the terminal velocity in an unbounded medium $U_{t\infty}$ is related to its counterpart in a confined medium U_t as follows: $U_t/U_{t\infty} = \alpha$, which implies that $U_t \propto (\rho_s - \rho_f)/\mu_f$. This is the proportionally relation we expect to find in our numerical experiments.

We will express our results in terms of the flow's Reynolds number Re and the drag coefficient C_D, which, for the problem at hand, are defined, respectively, as

$$\mathrm{Re} = (2R)\rho_f u_{Cy}/\mu_f \qquad \text{and} \qquad C_D = F_D \Big/ \left[\tfrac{1}{2}\rho_f\, u_{Cy}^2 (2R) L\right], \tag{65}$$

which can be shown to imply $C_D \propto 1/\mathrm{Re}$ (see, Jayaweera and Mason, 1965).

Referring to Fig. 10, in our numerical experiments we consider a disk B_t (representing the

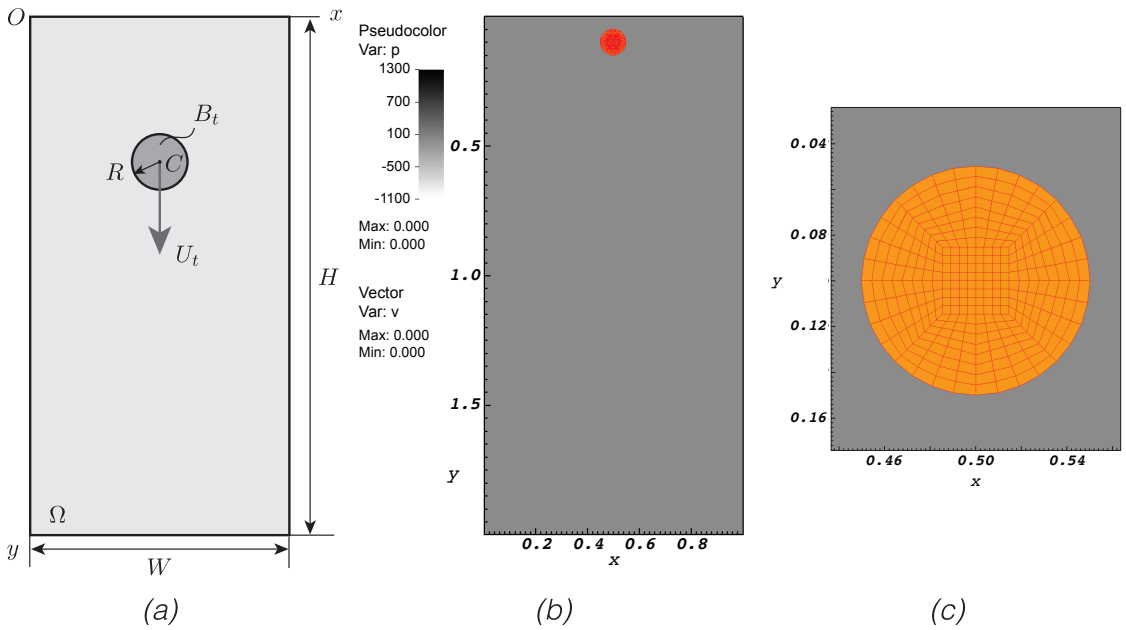

Figure 10: Vertical channel containing viscous fluid through which a small incompressible disk is descending: (a) system's geometry; (b) initial conditions (disk released from rest in a quiescent fluid); (c) detail of mesh of the immersed body. The disk's terminal velocity is denoted by U_t.

midplane of the cylinder), with radius R and center C, released from rest in an initially quiescent rectangular control volume Ω with height H and width W. As the disk sinks, we measure the

position of C and infer its velocity, denoted by u_{Cy}. When u_{Cy} achieves a (sufficiently) constant value, we refer to this value as the terminal velocity and denote it by U_{tN}. When $u_{Cy} = U_{tN}$ we also compute the drag coefficient C_{DN} of the disk. The latter is assumed to consists of an incompressible neo-Hookean material whose Piola stress is given by

$$\hat{\mathsf{P}}_{\mathrm{s}} = -p_{\mathrm{s}}\mathsf{I} + \mu^{e}\big(\mathsf{F} - \mathsf{F}^{-\mathrm{T}}\big). \tag{66}$$

The following parameters were used: $H = 2.0\,\mathrm{cm}$, $W = 1.0\,\mathrm{cm}$, $R = 0.05\,\mathrm{cm}$, $\rho_{\mathrm{f}} = 1.0\,\mathrm{g/cm^3}$, $\mu_{\mathrm{s}} = 0.0\,\mathrm{P}$, $\mu^{e} = 1 \times 10^{3}\,\mathrm{dyn/cm^2}$ and $g = 981\,\mathrm{cm/s^2}$. Two different cases were considered. In Case 1, the density of the solid was varied while the viscosity of the fluid was held constant at $\mu_{\mathrm{f}} = 1.0\,\mathrm{P}$. In Case 2, we used for different fluid viscosities while the density of the solid was held constant at $\rho_{\mathrm{s}} = 3.0\,\mathrm{g/cm^3}$. The values used for ρ_{s} and μ_{f} can be found in Table 3, which also lists

Table 3: Values of solid density and fluid density used for the tests. Also shown are the values obtained for the terminal velocity, Reynolds number and drag coefficient from these tests.

	$\rho_{\mathrm{s}}(\mathrm{g/cm^3})$	$\mu_{\mathrm{f}}(\mathrm{P})$	$U_{tN}(\mathrm{cm/s}$	Re_{tN}	C_{DtN}
Case 1	2.0	1.0	0.8179	0.082	230.3
	3.0	1.0	1.6270	0.163	116.4
	4.0	1.0	2.4412	0.244	77.6
Case 2	3.0	1.0	1.6270	0.163	116.4
	3.0	2.0	0.8236	0.041	454.4
	3.0	4.0	0.4137	0.010	1801.0
	3.0	8.0	0.2070	0.003	7192.5

the corresponding values of U_{tN}, Re_N, and C_{DtN}. We have used $\mathcal{Q}_0^2|\mathcal{Q}_0^1$ elements for the control volume and a Gauss quadrature rule of order 4 for assembling the operators defined over the solid domain. In all numerical experiments pertaining to Cases 1 and 2, we have used 16,384 cells and 181,250 DoFs for the control volume, and 320 cells and 2,626 DoFs for the solid.

The results for Case 1 are reported in Figs. 11 and 12, whereas those for Case 2 are reported

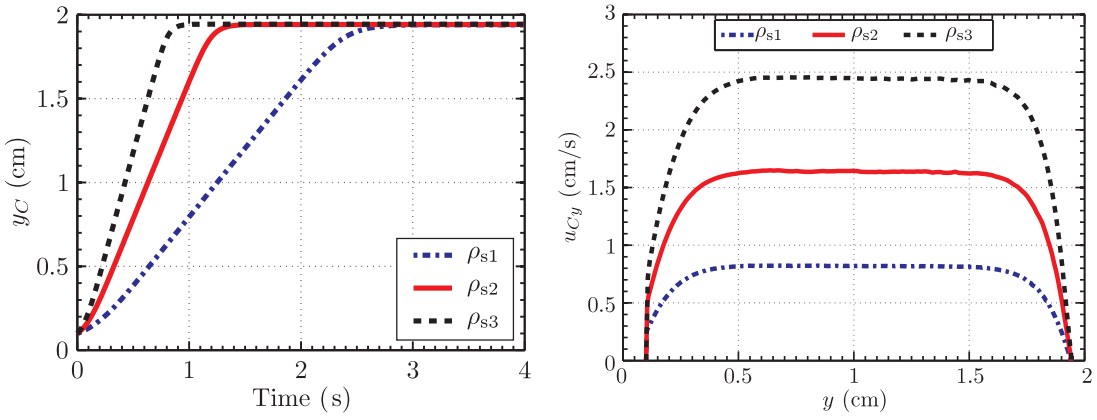

(a) Axial position of mass center of the disk

(b) Vertical velocity of mass center of the disk

Figure 11: Effect of changing the density of the solid on the motion of the center of mass of the cylinder. Note: $\rho_{\mathrm{s1}} = 2\,\mathrm{g/cm^3}$, $\rho_{\mathrm{s2}} = 3\,\mathrm{g/cm^3}$ and $\rho_{\mathrm{s3}} = 4\,\mathrm{g/cm^3}$.

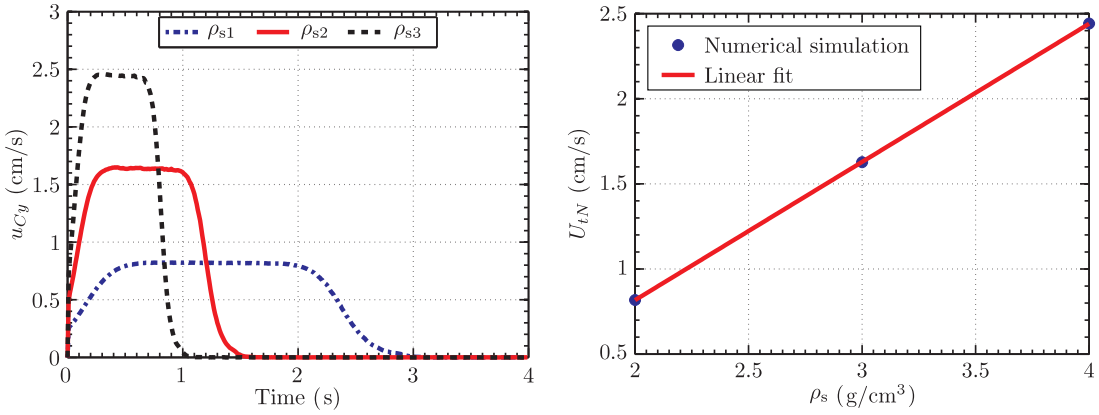

(a) Velocity of mass center of the cylinder versus time.
Note: $\rho_{s1} = 2\,\mathrm{g/cm^3}$, $\rho_{s2} = 3\,\mathrm{g/cm^3}$ and $\rho_{s3} = 4\,\mathrm{g/cm^3}$

(b) Terminal velocity of the cylinder as function of its density

Figure 12: Effect of changing the density of the cylinder on its terminal velocity.

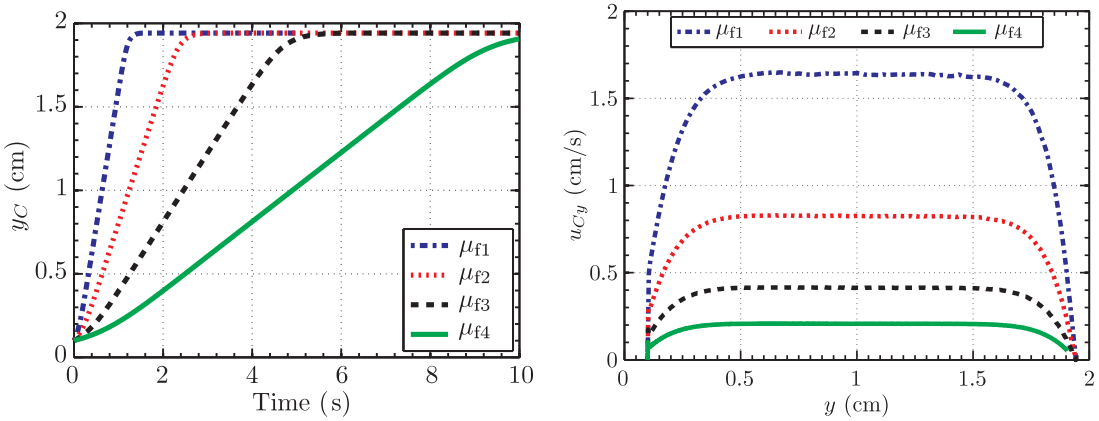

(a) Axial position of mass center of the disk

(b) Vertical velocity of mass center of the disk

Figure 13: Effect of changing the viscosity of the fluid on the motion of the center of mass of the cylinder. Note: $\mu_{f1} = 1.0\,\mathrm{P}$, $\mu_{f2} = 2.0\,\mathrm{P}$, $\mu_{f2} = 4.0\,\mathrm{P}$ and $\mu_{f4} = 8.0\,\mathrm{P}$.

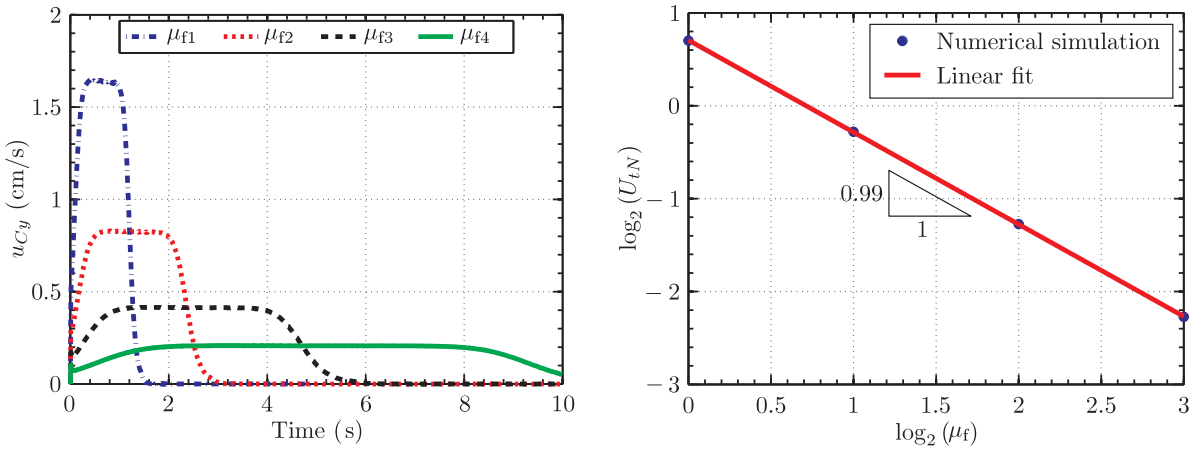

(a) Velocity of mass center of the cylinder versus time. (b) Terminal velocity of the cylinder as function of the viscosity of the fluid

Figure 14: Effect of fluid viscosity on the terminal velocity of the disk. Note: $\mu_{f1} = 1.0\,\mathrm{P}$, $\mu_{f2} = 2.0\,\mathrm{P}$, $\mu_{f2} = 4.0\,\mathrm{P}$ and $\mu_{f4} = 8.0\,\mathrm{P}$.

in Figs. 13 and 14. Figures 11(b) and 13(b) show that u_{Cy} increases over a distance of about $y < H/3$, remains constant over $H/3 < y < 2H/3$ and then decreases over the remaining length of the channel. This is in accordance with actual experimental observations (cf., Clift et al., 1978). From Figs. 12(a) and 14(a), we see that the disk's terminal velocity increases with its density and decreases with the increase in the fluid's viscosity. Moreover, from Fig. 12(b) we see that the terminal velocity is linearly proportional to the density of the disk, and from Fig. 14(b) we see that the terminal velocity is inversely proportional to the viscosity of the fluid, as expected. Finally, from Fig. 15 we see that the calculated drag coefficient at the terminal velocity C_{DtN} of the cylinder

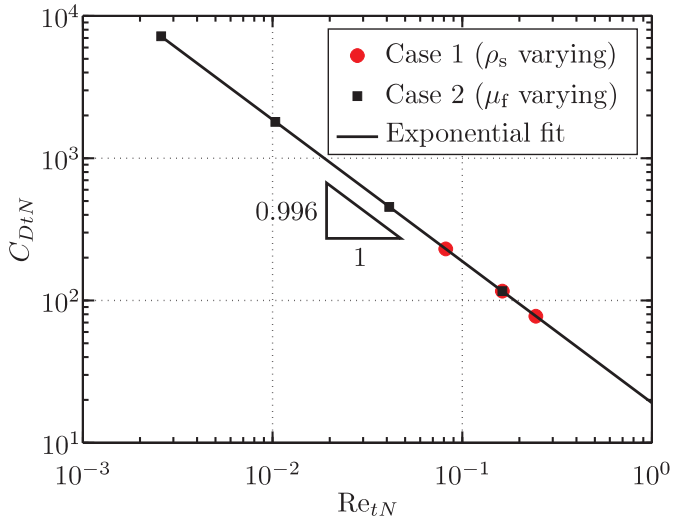

Figure 15: Drag coefficient versus Reynolds number (corresponding to the terminal velocity of the cylinder).

is indeed inversely proportional to the corresponding Reynolds number Re_{tN}.

We end this section with a few remarks on convergence and mesh refinement. The computed

value of the terminal velocity can be expected to be accurate only when the meshes are "sufficiently" refined. With this in mind, we considered the effect of mesh refinement on the the value of U_{tN} for Case 1 corresponding to $\rho_s = 4\,\mathrm{g/cm^3}$. Table 4 shows the mesh sizes for both the solid and the control volume along with the corresponding value of U_{tN}. The corresponding velocity of C as a

Table 4: Terminal velocity of the cylinder obtained from simulations using meshes having different global refinement levels.

	Solid		Control Volume		U_{tN} cm/s
	Cells	DoFs	Cells	DoFs	
Level 1	80	674	1,024	11,522	2.10
Level 2	80	674	4,096	45,570	2.37
Level 3	320	2,626	16,384	181,250	2.45
Level 4	1,280	10,370	65,536	722,946	2.50

function of time is shown in Fig. 16, in which we see that, as the meshes are refined, U_{tN} tends to

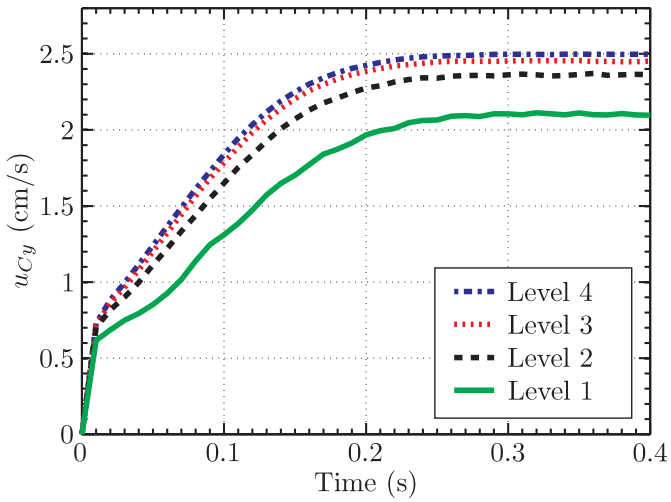

Figure 16: Effect of mesh refinement level on the terminal velocity of the mass center of the cylinder.

achieve a "converged" value. We note that the Case 1 and 2 results presented earlier correspond to Level 3 in Table 4.

5.3 Results for Compressible Immersed Solids

5.3.1 Compressible Annulus inflated by a Point source

We now present the first example pertaining to Problem 2 and its discrete counterpart Problem 5. Here we study the deformation of a hollow compressible cylinder submerged in a fluid contained in a rigid prismatic box due to the influx of fluid along the axis of the cylinder. Referring to Fig. 17, we consider a two-dimensional solid annulus with inner radius R and thickness w that is concentric with a fluid-filled square box of edge length l. A point mass source of fluid of constant strength Q is located at the center C of Ω. Because of this source, the balance of mass for the system is

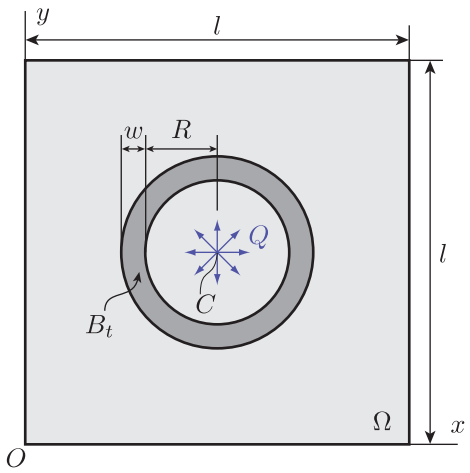

Figure 17: Initial configuration of an annulus immersed in a square box filled with fluid. At the center C of the box is a point source of constant strength Q.

modified as follows:

$$\int_\Omega q\left[\operatorname{div}\boldsymbol{u} + \frac{Q}{\rho_{\mathrm{f}}}\delta(\boldsymbol{x}-\boldsymbol{x}_C)\right]\mathrm{d}v - \int_{B_t} q\operatorname{div}\boldsymbol{u}\,\mathrm{d}v = 0, \tag{67}$$

where $\delta(\boldsymbol{x}-\boldsymbol{x}_C)$ denotes a Dirac-δ distribution centered at C. We apply homogeneous Dirichlet boundary conditions on $\partial\Omega$. The annulus was chosen to have a compressible Neo-Hookean elastic response given by

$$\hat{\mathsf{P}}^e_{\mathrm{s}} = \mu^e\big(\mathsf{F} - J^{-2\nu/(1-2\nu)}\mathsf{F}^{-\mathrm{T}}\big), \tag{68}$$

where μ^e is the shear modulus and ν is the Poisson's ratio for the solid. Since the solid is compressible both the volume of solid and that of the fluid in the control volume can change. However, since the fluid cannot leave the control volume, the amount of fluid volume increase must match the decrease in the volume of the solid. This implies that the difference in these two volumes can serve as an estimate of the numerical error incurred.

We have used the following parameters: $R = 0.25\,\mathrm{m}$, $w = 0.05\,\mathrm{m}$, $l = 1.0\,\mathrm{m}$, $\rho_{\mathrm{f}} = \rho_{\mathrm{s}_0} = 1\,\mathrm{kg/m^3}$, $\mu_{\mathrm{f}} = \mu_{\mathrm{s}} = 1\,\mathrm{Pa{\cdot}s}$, $\mu^e = 1\,\mathrm{Pa}$, $\nu = 0.3$, $Q = 0.1\,\mathrm{kg/s}$ and $dt = 0.01\,\mathrm{s}$. We have tested three different mesh refinement levels whose details have been listed in Table 5. The initial state of the system

Table 5: Number of cells and DoFs used in the different simulations involving the deformation of a compressible annulus under the action of a point source.

	Solid		Control Volume	
	Cells	DoFs	Cells	DoFs
Level 1	6,240	50,960	1,024	9,539
Level 2	24,960	201,760	4,096	37,507
Level 3	99,840	802,880	16,384	148,739

is shown in Fig. 18(a). As time progresses, the fluid entering the control volume deforms and compresses the annulus, whose configuration for $t = 1\,\mathrm{s}$ is shown in Fig. 18(b). Referring to Fig. 19,

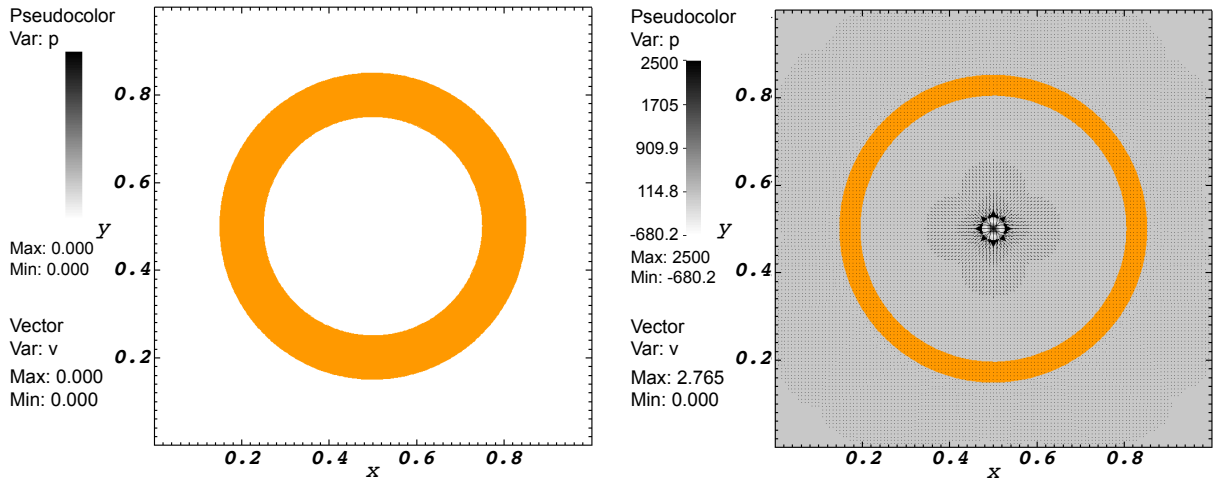

(a) $t = 0\,\mathrm{s}$ (b) $t = 1.0\,\mathrm{s}$

Figure 18: The velocity and the mean normal stress field over the control volume. Also shown is the annulus mesh.

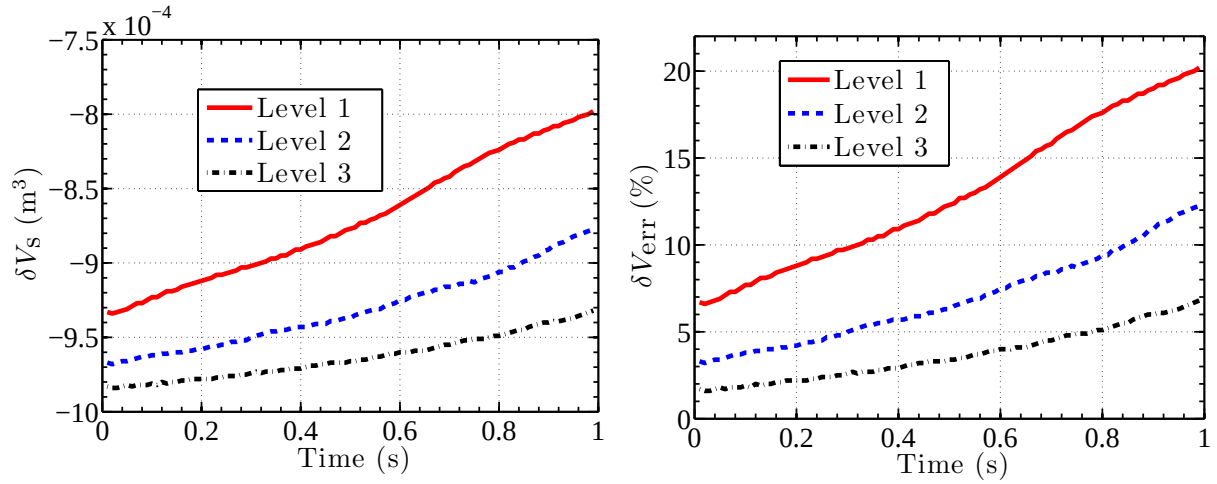

Figure 19: The difference between the instantaneous amount of fluid entering due to the source and the change in the area of the annulus. The difference reduces with mesh refinement.

when we look at the difference in the instantaneous amount of fluid entering the control volume and the decrease in the volume of the solid, we see that the difference increases over time. This is not surprising since the mesh of the solid becomes progressively distorted as the fluid emanating from the point source push the inner boundary of the annulus. As expected, the error significantly reduces with the increase in the refinements of the fluid and the solid meshes.

5.3.2 Elastic bar behind a cylinder

We now present a second example pertaining to Problem 2 and its discrete counterpart Problem 5. To test the interaction of a purely elastic compressible object in an incompressible linear viscous flow we consider the two non-steady FSI cases discussed by Turek and Hron (2006), referred to as FSI2 and FSI3, respectively. In presenting our results and to facilitate comparisons, we use the same geometry, nondimensionalization, and parameters used by Turek and Hron (2006). Specifically, referring to Fig. 20, the system consists of a 2D channel of dimensions $L = 2.5\,\mathrm{m}$ and height

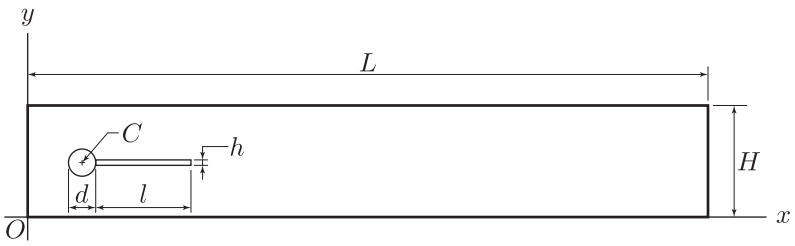

Figure 20: Solution domain for the problem of an elastic bar behind a cylinder.

$H = 0.41\,\mathrm{m}$, with a fixed circle K of diameter $d = 0.1\,\mathrm{m}$ and centered at $C = (0.2, 0.2)\,\mathrm{m}$. The elastic bar attached at the right edge of the circle has length $l = 0.35\,\mathrm{m}$ and height $h = 0.02\,\mathrm{m}$.

The constitutive response of the bar is that of a de Saint-Venant Kirchhoff material (Holzapfel, 2000; Turek and Hron, 2006). Hence, referring to Eq. (7), $\hat{\mathsf{T}}_{\mathrm{s}}^{v} = \mathsf{0}$ and

$$\hat{\mathsf{T}}_{\mathrm{s}}^{e} = J^{-1}\mathsf{F}\big[2\mu_{\mathrm{s}}^{e}\mathsf{E} + \lambda_{\mathrm{s}}^{e}(\mathrm{tr}\,\mathsf{E})\mathsf{I}\big]\mathsf{F}^{\mathrm{T}} = J^{-1}\mathsf{F}\left[2\mu_{\mathrm{s}}^{e}\mathsf{E} + \frac{2\mu_{\mathrm{s}}^{e}\nu_{\mathrm{s}}^{e}}{1-2\nu_{\mathrm{s}}^{e}}(\mathrm{tr}\,\mathsf{E})\mathsf{I}\right]\mathsf{F}^{\mathrm{T}}, \tag{69}$$

where $\mathsf{E} = (\mathsf{F}^{\mathrm{T}}\mathsf{F} - \mathsf{I})/2$ is the Lagrangian strain tensor, μ_{s}^{e} and λ_{s}^{e} are the Lamé elastic constants of the immersed solid, and where $\nu_{\mathrm{s}}^{e} = \lambda_{\mathrm{s}}^{e}/[2(\lambda_{\mathrm{s}}^{e} + \mu_{\mathrm{s}}^{e})]$ is corresponding Poisson's ratio.

The system is initially at rest. The boundary conditions are such that there is no slip over the top and bottom surfaces of the channel as well as over the surface of the circle (the immersed solid does not slip relative to the fluid). At the right end of the channel we impose "do nothing" boundary conditions. Using the coordinate system indicated in Fig. 20, at the left end of the channel we impose the following distribution of inflow velocity:

$$u_x = 1.5\bar{U}\,4y(H-y)/H^2 \quad \text{and} \quad u_y = 0, \tag{70}$$

where $\bar{U}$ is a constant with dimension of speed.

The constitutive parameters and the the parameter $\bar{U}$ used in the simulations are reported in Table 6, in which we have also indicated the flow's Reynolds number.

The outcome of the numerical benchmark proposed by Turek and Hron (2006) is typically expressed (i) in terms of the time dependent position of the the midpoint A at the right end of the elastic bar, and (ii) in terms of the force acting on the boundary S of the union of the circle K and the elastic bar B_t (see Fig. 21). Denoting by $\hat{\imath}$ and $\hat{\jmath}$ the orthonormal base vectors associated with

Table 6: Parameters used in the two non-steady FSI cases in Turek and Hron (2006).

Parameter	FSI2	FSI3
$\rho_{\rm s}\,(10^3\,{\rm kg/m^3})$	10.0	1.0
$\nu_{\rm s}^e$	0.4	0.4
$\mu_{\rm s}^e\,[10^6\,{\rm kg/(m{\cdot}s^2)}]$	0.5	2.0
$\rho_{\rm f}\,(10^3\,{\rm kg/m^3})$	1.0	1.0
$\mu_{\rm f}\,(10^{-3}\,{\rm m^2/s})$	1.0	1.0
$\bar{U}\,({\rm m/s})$	1.0	2.0
$\rho_{\rm s}/\rho_{\rm f}$	10.0	1.0
${\rm Re} = \bar{U}d/\mu_{\rm f}$	100.0	200.0

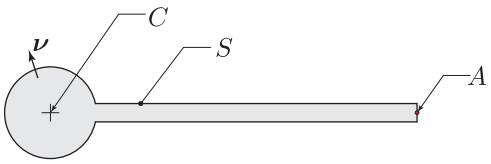

Figure 21: Domain resulting from the union of the elastic bar B_t and the fixed circle K with center C. $S = \partial(K \cup B_t)$ denotes the boundary of the domain in question and it is oriented by the unit normal $\boldsymbol{\nu}$. Point A is the midpoint on the right boundary of the elastic bar.

the x and y axes, respectively, the force acting on the domain S is

$$F_D\,\hat{\imath} + F_L\,\hat{\jmath} = \int_S \mathsf{T}\boldsymbol{\nu}\,{\rm d}a, \tag{71}$$

where F_D and F_L are the lift and drag, respectively, and where $\mathsf{T}\boldsymbol{\nu}$ is the (time dependent) traction vector acing on S. As remarked by Turek and Hron (2006) there are several ways to evaluate the right-hand side of Eq. (71). For example, the traction on the elastic bar could be calculated on the fluid side or on the solid side or even as an average of these values.* However, we need to keep in mind that we use a single field for the Lagrange multiplier p and that this field is expected to be discontinuous across the across the (moving) boundary of the immersed object. In turn, this means that the measure of the hydrodynamic force on S via a direct application of Eq. (71) would be adversely affected by the oscillations in the field p across S. With this in mind, referring to Eq. (2), we observe that a straightforward application of the divergence theorem over the domain $\Omega \setminus (K \cup B_t)$ yields the following result:

$$F_D\,\hat{\imath} + F_L\,\hat{\jmath} = \int_{\partial\Omega} \mathsf{T}\boldsymbol{n}\,{\rm d}a - \int_{\Omega\setminus(K\cup B_t)} \rho\left\{\boldsymbol{b} - \left[\frac{\partial \boldsymbol{u}}{\partial t} + (\nabla\boldsymbol{u})\boldsymbol{u}\right]\right\}{\rm d}v, \tag{72}$$

where $\boldsymbol{n}$ denotes the outward unit normal of $\partial\Omega$. The estimation of the lift and drag over S via Eq. (72) is significantly less sensitive to the oscillations of the field p near the boundary of the immersed domain and this is the way we have measured F_D and F_L.

For both the FSI2 and FSI3 benchmarks, we performed calculations using 2,992 $\mathcal{Q}_0^2|\mathcal{Q}_0^1$ elements for the fluid and 704 $\mathcal{Q}_0^2$ elements for the immersed elastic bar. The number of degrees of freedom distributed over the control volume is 24,464 for the velocity and 3,124 for the pressure. The

*Ideally, the traction value computed on the solid and fluid sides are the same.

number of degrees of freedom distributed over the elastic bar is 6,018. The time step size for the FSI2 benchmark was set to 0.005 s, whereas the time step size for the FSI3 results was set to 0.001 s.

The results for the FSI2 case are shown in Figures 22 and 23 displaying the components of the displacement of point A and the components of the hydrodynamic force on S, respectively. The

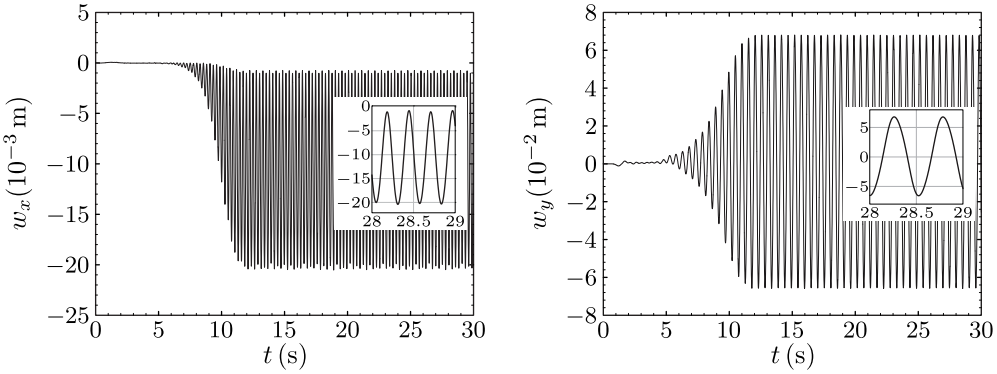

Figure 22: Nondimensional displacement of the midpoint at the right end of the elastic bar vs. time. The horizontal and vertical components of the displacement are plotted to the left and to the right, respectively.

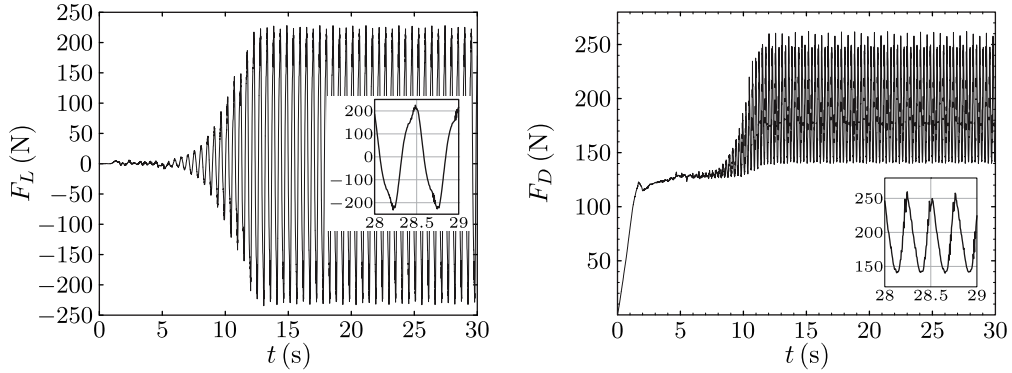

Figure 23: Plots of the lift (left) and drag (right) that the fluid exerts on the immersed fixed cylinder and the elastic bar.

analogous results for the FSI3 case are displayed in Figs. 24 and 25. As can be seen in these figures, the displacement values as well as the lift and drag results compare rather favorably with those in the benchmark proposed by Turek and Hron (2006), especially when considering that our integration scheme is the implicit Euler method.

6 Summary and Conclusions

In this paper we have presented the first set of results meant to provide a validation of the fully variational FEM approach to an immersed method for FSI problems presented in Heltai and Costanzo (2012). The results presented herein, while still incomplete, show that the proposed formulation can be an effective and accurate method in the solution of FSI problems in which the solid body is fully immersed in the fluid. The results show that the proposed approach can be applied to a wide variety of problems in which the immersed solid need not have the same density or the same

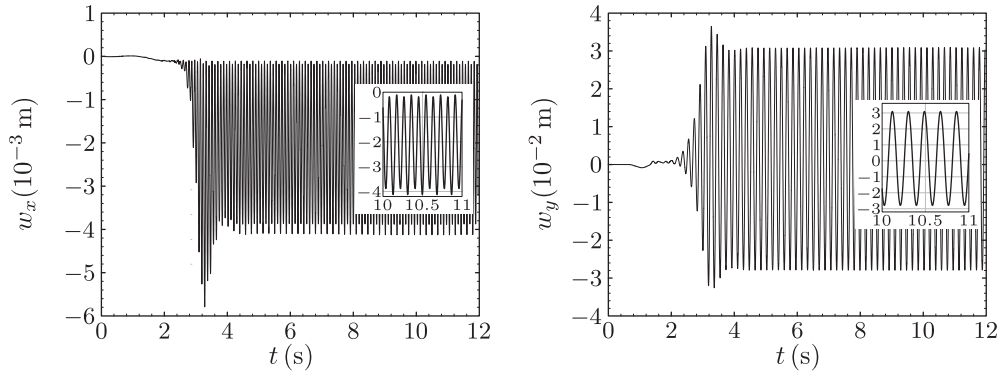

Figure 24: Nondimensional displacement of the midpoint at the right end of the elastic bar vs. time. The horizontal and vertical components of the displacement are plotted to the left and to the right, respectively.

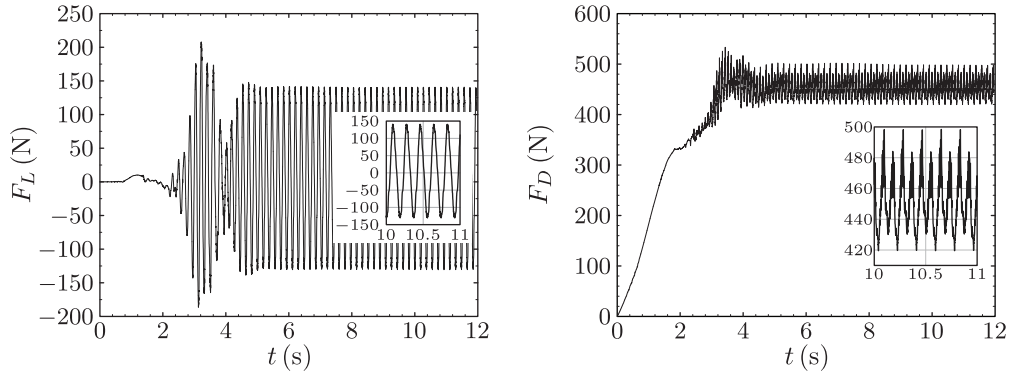

Figure 25: Plots of the lift (left) and drag (right) that the fluid exerts on the immersed fixed cylinder and the elastic bar.

viscous response as the surrounding fluid. Furthermore, as shown by the results concerning the lid cavity problem, the proposed computational approach can be applied to problems with very large deformations without any need to adjust the meshes used for either the control volume or the immersed solid. In the future, we plan to extend these results to include the full set of validation tests discussed by Turek and Hron (2006) and discuss details of the calculation along with possible strategies to improve the issue pertaining to conservation of volume for the immersed domain.

Acknowledgements

The research leading to these results has received specific funding under the "Young SISSA Scientists' Research Projects" scheme 2011-2012, promoted by the International School for Advanced Studies (SISSA), Trieste, Italy.

Appendix: Definition of the operators used in the dual formulation

In the statement of Problem 1 we have used the following operators:

$$\mathcal{M}_{\alpha 1} : \mathscr{H}_V \to \mathscr{V}^*, \qquad {}_{\mathscr{V}^*}\langle \mathcal{M}_{\alpha 1}\boldsymbol{u}, \boldsymbol{v}\rangle_{\mathscr{V}} := \int_\Omega \rho_\mathrm{f}\, \boldsymbol{u}\cdot\boldsymbol{v}\,\mathrm{d}v \qquad \forall \boldsymbol{u}\in\mathscr{H}_V, \forall \boldsymbol{v}\in\mathscr{V}_0, \tag{73}$$

$$\mathcal{N}_{\alpha 1}(\boldsymbol{u}) : \mathscr{V} \to \mathscr{V}^*, \qquad {}_{\mathscr{V}^*}\big\langle \mathcal{N}_{\alpha 1}(\boldsymbol{u})\boldsymbol{w}, \boldsymbol{v}\big\rangle_{\mathscr{V}} := \int_\Omega \rho_{\mathrm{f}} (\nabla_{\boldsymbol{x}} \boldsymbol{w})\boldsymbol{u} \cdot \boldsymbol{v} \,\mathrm{d}v \quad \forall \boldsymbol{u}, \boldsymbol{w} \in \mathscr{V}, \forall \boldsymbol{v} \in \mathscr{V}_0, \tag{74}$$

$$\mathcal{D}_{\alpha 1} : \mathscr{V} \to \mathscr{V}^*, \qquad {}_{\mathscr{V}^*}\big\langle \mathcal{D}_{\alpha 1}\boldsymbol{u}, \boldsymbol{v}\big\rangle_{\mathscr{V}} := \int_\Omega \hat{\mathsf{T}}^v_{\mathrm{f}}[\boldsymbol{u}] \cdot \nabla_{\boldsymbol{x}} \boldsymbol{v} \,\mathrm{d}v \quad \forall \boldsymbol{u} \in \mathscr{V}, \forall \boldsymbol{v} \in \mathscr{V}_0, \tag{75}$$

$$\mathcal{B}_{\beta 1} : \mathscr{V} \to \mathscr{Q}^*, \qquad {}_{\mathscr{Q}^*}\big\langle \mathcal{B}_{\beta 1}\boldsymbol{u}, q\big\rangle_{\mathscr{Q}} := -\int_\Omega q \,\mathrm{div}\, \boldsymbol{u} \,\mathrm{d}v \quad \forall q \in \mathscr{Q}, \forall \boldsymbol{u} \in \mathscr{V}, \tag{76}$$

$$\mathcal{B}^{\mathrm{T}}_{\beta 1} : \mathscr{Q} \to \mathscr{V}^*, \qquad {}_{\mathscr{V}^*}\big\langle \mathcal{B}^{\mathrm{T}}_{\beta 1} q, \boldsymbol{u}\big\rangle_{\mathscr{V}} := -\int_\Omega q \,\mathrm{div}\, \boldsymbol{u} \,\mathrm{d}v \quad \forall q \in \mathscr{Q}, \forall \boldsymbol{u} \in \mathscr{V}. \tag{77}$$

The operators defined in Eqs. (73)–(77) concern terms that are typical of the Navier-Stokes equations and will be referred to as the Navier-Stokes component of the problem. As in other immersed methods, these operators have their support in Ω as a whole.

We now define those operators in our formulation that have their support over B but do not contain prescribed body forces or boundary terms.

$$\begin{aligned}
&\delta\mathcal{M}_{\alpha 1}(\boldsymbol{w}) : \mathscr{H}_V \to \mathscr{V}^*, \ \forall \boldsymbol{w} \in \mathscr{Y}, \forall \boldsymbol{u} \in \mathscr{H}_V, \forall \boldsymbol{v} \in \mathscr{V}_0, \\
&\qquad {}_{\mathscr{V}^*}\big\langle \delta\mathcal{M}_{\alpha 1}(\boldsymbol{w})\boldsymbol{u}, \boldsymbol{v}\big\rangle_{\mathscr{V}} := \int_B \big\{ \big(\rho_{\mathrm{s}_0}(\boldsymbol{s}) - \rho_{\mathrm{f}} J[\boldsymbol{w}]\big)\boldsymbol{u}(\boldsymbol{x}) \cdot \boldsymbol{v}(\boldsymbol{x}) \big\}_{\boldsymbol{x}=\boldsymbol{s}+\boldsymbol{w}(\boldsymbol{s})} \,\mathrm{d}V,
\end{aligned} \tag{78}$$

$$\begin{aligned}
&\delta\mathcal{N}_{\alpha 1}(\boldsymbol{w}, \boldsymbol{\ell}, \boldsymbol{z}) : \mathscr{V} \to \mathscr{V}^*, \ \forall \boldsymbol{w}, \boldsymbol{\ell} \in \mathscr{Y}, \forall \boldsymbol{u}, \boldsymbol{z} \in \mathscr{V}, \forall \boldsymbol{v} \in \mathscr{V}_0, \\
&\qquad {}_{\mathscr{V}^*}\big\langle \delta\mathcal{N}_{\alpha 1}(\boldsymbol{w}, \boldsymbol{\ell}, \boldsymbol{z})\boldsymbol{u}, \boldsymbol{v}\big\rangle_{\mathscr{V}} := \int_B \big\{ \big[(\rho_{\mathrm{s}_0}(\boldsymbol{s}) \nabla_{\boldsymbol{x}} \boldsymbol{u}(\boldsymbol{x}) \boldsymbol{\ell}(\boldsymbol{s}) \\
&\qquad\qquad - \rho_{\mathrm{f}} J[\boldsymbol{w}] \nabla_{\boldsymbol{x}} \boldsymbol{u}(\boldsymbol{x}) \boldsymbol{z}(\boldsymbol{x}) \big] \cdot \boldsymbol{v}(\boldsymbol{x}) \big\}_{\boldsymbol{x}=\boldsymbol{s}+\boldsymbol{w}(\boldsymbol{s})} \,\mathrm{d}V.
\end{aligned} \tag{79}$$

$$\begin{aligned}
&\delta\mathcal{D}_{\alpha 1}(\boldsymbol{w}) : \mathscr{V} \to \mathscr{V}^*, \ \forall \boldsymbol{w} \in \mathscr{Y}, \forall \boldsymbol{u} \in \mathscr{V}, \forall \boldsymbol{v} \in \mathscr{V}_0, \\
&\qquad {}_{\mathscr{V}^*}\big\langle \delta\mathcal{D}_{\alpha 1}(\boldsymbol{w})\boldsymbol{u}, \boldsymbol{v}\big\rangle_{\mathscr{V}} := \int_B \Big[J[\boldsymbol{w}] \big(\hat{\mathsf{T}}^v_{\mathrm{s}}[\boldsymbol{u}] - \hat{\mathsf{T}}^v_{\mathrm{f}}[\boldsymbol{u}] \big) \cdot \nabla_{\boldsymbol{x}} \boldsymbol{v}(\boldsymbol{x}) \Big]_{\boldsymbol{x}=\boldsymbol{s}+\boldsymbol{w}(\boldsymbol{s})} \,\mathrm{d}V,
\end{aligned} \tag{80}$$

$$\begin{aligned}
&\mathcal{A}_\alpha(\boldsymbol{w}, \boldsymbol{h}) \in \mathscr{V}^*, \ \forall \boldsymbol{w}, \boldsymbol{h} \in \mathscr{Y}, \forall \boldsymbol{v} \in \mathscr{V}_0 \\
&\qquad {}_{\mathscr{V}^*}\big\langle \mathcal{A}_\alpha(\boldsymbol{w}, \boldsymbol{h}), \boldsymbol{v}\big\rangle_{\mathscr{V}} := \int_B \big[\hat{\mathsf{P}}^e_{\mathrm{s}}[\boldsymbol{w}] \mathsf{F}^{\mathrm{T}}[\boldsymbol{h}] \cdot \nabla_{\boldsymbol{x}} \boldsymbol{v}(\boldsymbol{x}) \big]_{\boldsymbol{x}=\boldsymbol{s}+\boldsymbol{h}(\boldsymbol{s})} \,\mathrm{d}V.
\end{aligned} \tag{81}$$

We now define operators with support in B that express the coupling of the velocity fields defined over Ω and over B. Specifically, we have

$$\begin{aligned}
&\mathcal{M}_{\gamma 3} : \mathscr{H}_Y \to \mathscr{H}_Y^*, \ \forall \boldsymbol{w}, \boldsymbol{y} \in \mathscr{H}_Y, \\
&\qquad {}_{\mathscr{H}_Y^*}\big\langle \mathcal{M}_{\gamma 3}\boldsymbol{w}, \boldsymbol{y}\big\rangle_{\mathscr{H}_Y} := \Phi_B \int_B \boldsymbol{w} \cdot \boldsymbol{y}(\boldsymbol{s}) \,\mathrm{d}V,
\end{aligned} \tag{82}$$

$$\begin{aligned}
&\mathcal{M}_{\gamma 1}(\boldsymbol{w}) : \mathscr{V} \to \mathscr{H}_Y^*, \ \forall \boldsymbol{u} \in \mathscr{V}, \forall \boldsymbol{w} \in \mathscr{Y}, \forall \boldsymbol{y} \in \mathscr{H}_Y, \\
&\qquad {}_{\mathscr{H}_Y^*}\big\langle \mathcal{M}_{\gamma 1}(\boldsymbol{w})\boldsymbol{u}, \boldsymbol{y}\big\rangle_{\mathscr{H}_Y} := \Phi_B \int_B \boldsymbol{u}(\boldsymbol{x})\big|_{\boldsymbol{x}=\boldsymbol{s}+\boldsymbol{w}(\boldsymbol{s})} \cdot \boldsymbol{y}(\boldsymbol{s}) \,\mathrm{d}V
\end{aligned} \tag{83}$$

$$\begin{aligned}
&\mathcal{M}^{\mathrm{T}}_{\gamma 1}(\boldsymbol{w}) : \mathscr{H}_Y \to \mathscr{V}^*, \ \forall \boldsymbol{u} \in \mathscr{V}, \forall \boldsymbol{w} \in \mathscr{Y}, \forall \boldsymbol{y} \in \mathscr{H}_Y \\
&\qquad {}_{\mathscr{V}^*}\big\langle \mathcal{M}^{\mathrm{T}}_{\gamma 1}(\boldsymbol{w})\boldsymbol{y}, \boldsymbol{u}\big\rangle_{\mathscr{V}} := \Phi_B \int_B \boldsymbol{u}(\boldsymbol{x})\big|_{\boldsymbol{x}=\boldsymbol{s}+\boldsymbol{w}(\boldsymbol{s})} \cdot \boldsymbol{y}(\boldsymbol{s}) \,\mathrm{d}V
\end{aligned} \tag{84}$$

Finally, we define the operators that express the action of prescribed body and surface forces.

$$\begin{aligned}
&\mathcal{F}_\alpha \in \mathscr{V}^*, \ \forall \boldsymbol{b} \in H^{-1}(\Omega), \forall \boldsymbol{\tau}_g \in H^{-\frac{1}{2}}(\partial\Omega_N), \forall \boldsymbol{v} \in \mathscr{V}_0 \\
&\qquad {}_{\mathscr{V}^*}\big\langle \mathcal{F}_\alpha, \boldsymbol{v}\big\rangle_{\mathscr{V}} := \int_\Omega \rho_{\mathrm{f}}\, \boldsymbol{b} \cdot \boldsymbol{v} \,\mathrm{d}v + \int_{\partial\Omega_N} \boldsymbol{\tau}_g \cdot \boldsymbol{v} \,\mathrm{d}a
\end{aligned} \tag{85}$$

$$\begin{aligned}
&\mathcal{G}_\alpha(\boldsymbol{w}) \in \mathscr{V}^*,\ \forall \boldsymbol{w} \in \mathscr{Y}, \forall \boldsymbol{b} \in H^{-1}(\Omega), \forall \boldsymbol{v} \in \mathscr{V}_0 \\
&\qquad {}_{\mathscr{V}^*}\big\langle \mathcal{G}_\alpha(\boldsymbol{w}), \boldsymbol{v} \big\rangle_{\mathscr{V}} := \int_B \big(\rho_{\mathrm{s}_0}(\boldsymbol{s}) - \rho_{\mathrm{f}} J[\boldsymbol{w}]\big)\boldsymbol{b} \cdot \boldsymbol{v}(\boldsymbol{x})\big|_{\boldsymbol{x}=\boldsymbol{s}+\boldsymbol{w}(\boldsymbol{s})}\, \mathrm{d}v.
\end{aligned} \tag{86}$$

Additional operators used in the dual formulation for the compressible case

$$\begin{aligned}
&\delta\mathcal{B}_{\beta 1}(\boldsymbol{w}) : \mathscr{V} \to \mathscr{Q}^*,\ \forall \boldsymbol{w}, \in \mathscr{Y}, \forall \boldsymbol{u} \in \mathscr{V}, \forall q \in \mathscr{Q} \\
&\qquad {}_{\mathscr{Q}^*}\big\langle \delta\mathcal{B}_{\beta 1}(\boldsymbol{w})\boldsymbol{u}, q \big\rangle_{\mathscr{Q}} := \int_B J[\boldsymbol{w}] q(\boldsymbol{x}) \operatorname{div} \boldsymbol{u}(\boldsymbol{x})\big|_{\boldsymbol{x}=\boldsymbol{s}+\boldsymbol{w}(\boldsymbol{s})}\, \mathrm{d}V,
\end{aligned} \tag{87}$$

$$\begin{aligned}
&\delta\mathcal{B}^{\mathrm{T}}_{\beta 1}(\boldsymbol{w}) : \mathscr{Q} \to \mathscr{V}^*,\ \forall \boldsymbol{w}, \in \mathscr{Y}, \forall p \in \mathscr{Q}, \forall \boldsymbol{v} \in \mathscr{V}_0 \\
&\qquad {}_{\mathscr{V}^*}\big\langle \delta\mathcal{B}^{\mathrm{T}}_{\beta 1}(\boldsymbol{w})p, \boldsymbol{v} \big\rangle_{\mathscr{V}} := \int_B J[\boldsymbol{w}] p(\boldsymbol{x}) \operatorname{div} \boldsymbol{v}(\boldsymbol{x})\big|_{\boldsymbol{x}=\boldsymbol{s}+\boldsymbol{w}(\boldsymbol{s})}\, \mathrm{d}V,
\end{aligned} \tag{88}$$

$$\begin{aligned}
&\delta\mathcal{P}_{\beta 2}(\boldsymbol{w}) : \mathscr{Q} \to \mathscr{Q}^*,\ \forall p, q \in \mathscr{Q}, \forall \boldsymbol{w} \in \mathscr{Y} \\
&\qquad {}_{\mathscr{Q}^*}\big\langle \delta\mathcal{P}_{\beta 2}(\boldsymbol{w})p, q \big\rangle_{\mathscr{Q}} := \int_B J[\boldsymbol{w}] p(\boldsymbol{x}) q(\boldsymbol{x})\big|_{\boldsymbol{x}=\boldsymbol{s}+\boldsymbol{w}(\boldsymbol{s})}\, \mathrm{d}V,
\end{aligned} \tag{89}$$

$$\begin{aligned}
&\delta\mathcal{E}_\beta(\boldsymbol{u}, \boldsymbol{w}, \boldsymbol{h}) \in \mathscr{Q}^*,\ \forall \boldsymbol{u} \in \mathscr{V}, \forall \boldsymbol{w}, \boldsymbol{h} \in \mathscr{Y} \\
&\qquad {}_{\mathscr{Q}^*}\big\langle \delta\mathcal{E}_\beta(\boldsymbol{u}, \boldsymbol{w}, \boldsymbol{h}), q \big\rangle_{\mathscr{Q}} := -\int_B \frac{1}{\operatorname{tr} \mathsf{I}} \Big[J[\boldsymbol{h}] \hat{\mathsf{T}}^v_{\mathrm{s}}[\boldsymbol{u}] \cdot \mathsf{I} + \hat{\mathsf{P}}^e_{\mathrm{s}}[\boldsymbol{w}] \cdot \mathsf{F}[\boldsymbol{h}] \Big] q(\boldsymbol{x})\big|_{\boldsymbol{x}=\boldsymbol{s}+\boldsymbol{h}(\boldsymbol{s})}\, \mathrm{d}V.
\end{aligned} \tag{90}$$

References

Boffi, D. and L. Gastaldi (2003) "A Finite Element Approach for the Immersed Boundary Method," *Computers & Structures*, **81**(8–11), pp. 491–501.

Boffi, D., L. Gastaldi, L. Heltai, and C. S. Peskin (2008) "On the Hyper-Elastic Formulation of the Immersed Boundary Method," *Computer Methods in Applied Mathematics and Engineering*, **197**(25–28), pp. 2210–2231.

Brenner, H. (1962) "Effect of Finite Boundaries on the Stokes Resistance of an Arbitrary Particle," *Journal of Fluid Mechanics*, **12**(01), pp. 35–48.

Brezzi, F. and M. Fortin (1991) *Mixed and Hybrid Finite Element Methods*, vol. 15 of *Springer Series in Computational Mathematics*, Springer-Verlag, New York.

Clift, R., J. R. Grace, and M. E. Weber (1978) *Bubbles, Drops, and Particles*, Academic Press, New York.

Davis, T. A. (2004) "Algorithm 832: UMFPACK V4.3—An Unsymmetric-Pattern Multifrontal Method," *ACM Transactions on Mathematical Software (TOMS)*, **30**(2), pp. 196–199.

Griffith, B. E. (2012) "On the Volume Conservation of the Immersed Boundary Method," *Communications in Computational Physics*, **12**(2), pp. 401–432.

Griffith, B. E. and X. Luo (2012) "Hybrid Finite Difference/Finite Element Version of the Immersed Boundary Method," *International Journal for Numerical Methods in Engineering*, submitted for publication.

Gurtin, M. E., E. Fried, and L. Anand (2010) *The Mechanics and Thermodynamics of Continua*, Cambridge University Press, New York.

Heltai, L. (2006) *The Finite Element Immersed Boundary Method*, Ph.D. thesis, Università di Pavia.

——— (2008) "On the Stability of the Finite Element Immersed Boundary Method," *Computers & Structures*, **86**(7–8), pp. 598–617.

Heltai, L. and F. Costanzo (2012) "Variational Implementation of Immersed Finite Element Methods," *Computer Methods in Applied Mechanics and Engineering*, **229–232**, pp. 110–127, DOI: 10.1016/j.cma.2012.04.001.

Heltai, L., S. Roy, and F. Costanzo (2012) "A Fully Coupled Immersed Finite Element Method for Fluid-Structure Interaction via the Deal.II Library," *Archive of Numerical Software*, submitted for publication and currently available through arXiv.org: arXiv:1209.2811.

Holzapfel, G. A. (2000) *Nonlinear Solid Mechanics*, John Wiley & Sons, Ltd., Chichester.

Jayaweera, K. O. L. F. and B. J. Mason (1965) "The Behaviour of Freely Falling Cylinders and Cones in a Viscous Fluid," *Journal of Fluid Mechanics*, **22**(04), pp. 709–720.

Peskin, C. S. (1977) "Numerical Analysis of Blood Flow in the Heart," *Journal of Computational Physics*, **25**(3), pp. 220–252.

——— (2002) "The Immersed Boundary Method," *Acta Numerica*, **11**, pp. 479–517.

Turek, S. and J. Hron (2006) "Proposal for Numerical Benchmarking of Fluid-Structure Interaction Between an Elastic Object and Laminar Incompressible Flow," in *Fluid-Structure Interaction* (H.-J. Bungartz and M. Schäfer, eds.), vol. 53 of *Lecture Notes in Computational Science and Engineering*, Springer, Berlin, Heidelberg, pp. 371–385, DOI: 10.1007/3-540-34596-5_15.

Wang, X. and W. K. Liu (2004) "Extended Immersed Boundary Method using FEM and RKPM," *Computer Methods in Applied Mechanics and Engineering*, **193**(12–14), pp. 1305–1321.

Wang, X. and L. Zhang (2010) "Interpolation Functions in the Immersed Boundary and Finite Element Methods," *Computational Mechanics*, **45**, pp. 321–334.

Zhang, L., A. Gerstenberger, X. Wang, and W. K. Liu (2004a) "Immersed Finite Element Method," *Computer Methods in Applied Mechanics and Engineering*, **193**(21–22), pp. 2051–2067.

Zhang, L. T. and M. Gay (2007) "Immersed Finite Element Method for Fluid-Structure Interactions," *Journal of Fluids and Structures*, **23**(6), pp. 839–857.

Zhang, L. T., A. Gerstenberger, X. Wang, and W. K. Liu (2004b) "Immersed Finite Element Method," *Computer Methods In Applied Mechanics and Engineering*, **193**(21-22), pp. 2051–2067.